



C- and L-band SAR signatures of Arctic sea ice during freeze-up

Mallik S. Mahmud^{a,b,*}, Vishnu Nandan^{c,a}, Suman Singha^{b,a}, Stephen E.L. Howell^d,
Torsten Geldsetzer^a, John Yackel^a, Benoit Montpetit^e

^a University of Calgary, Calgary, AB, Canada

^b German Aerospace Center (DLR), Bremen, Germany

^c Centre for Earth Observation Science (CEOS), University of Manitoba, Winnipeg, MB, Canada

^d Environment and Climate Change Canada, Toronto, ON, Canada

^e Environment and Climate Change Canada, Ottawa, ON, Canada

ARTICLE INFO

Edited by Menghua Wang

Keywords:

Arctic
New ice
SAR
Classification
L-band
C-band
Dual-frequency

ABSTRACT

Identifying sea ice types in the early stages of development from L-band SAR imagery remains an active research area during the Arctic freeze-up period. We used ScanSAR C- and L-band imagery from RADARSAT-2, ALOS PALSAR and ALOS-2 PALSAR-2, to identify ice types in the North Water Polynya (NOW) and Victoria Strait (VS) region of the Canadian Arctic. We investigated the HH-polarized microwave backscatter coefficient (σ_{HH}^0) and its GLCM texture parameters for six ice classes and open water. We found very low σ_{HH}^0 for nilas at both C- and L-band. Although similar σ_{HH}^0 found for grey ice at both frequencies, σ_{HH}^0 decrease with increasing ice thickness at L-band from grey ice, whereas, at C-band, σ_{HH}^0 increases from grey to grey-white ice and then decreases as the ice grows. GLCM texture parameters show lower values for L-band than C-band; however, separability among classes was found only for a few selected parameters. We used the support vector machine (SVM) algorithm for ice type classification from SAR scenes using σ_{HH}^0 and GLCM texture statistics. Due to overlapping σ_{HH}^0 signatures at C-band, early-stage ice classes were substantially misclassified. L-band identified early-stage ice classes with higher accuracy compared to C-band but misclassified thicker ice types and open water. L-band alone provided very good classification results (~80% accuracy) and combining L- and C-band (i.e., dual-frequency approach) further increased accuracy to >90%. C-band alone resulted in the lowest accuracy of <60%. We acknowledge that developing a universal ice classification is still a challenge and requires some manual supervision to adopt variable ice conditions into the classification method. However, a dual-frequency approach can achieve higher classification accuracy than conventionally used single-frequency approaches. This research highlights the value of upcoming L-Band SAR missions to improve sea ice classification in regions where a variety of ice types exist, including many thinner types, which are now dominating an increasingly warming Arctic.

1. Introduction

Due to anthropogenic warming, significant changes in the Arctic climate system have been observed (Jansen et al., 2020). These changes have resulted in a new Arctic sea ice regime where a substantial reduction in Arctic sea ice extent, thickness and concentration are apparent along with an extended melt season (Stroeve and Notz, 2018). In addition, the pre-dominant Arctic sea ice type has transitioned from thicker multiyear ice (MYI) to a new regime consisting of thinner first-year ice (FYI) (Comiso, 2012; Kwok, 2018). Model simulations indicate that the expanding coverage of open water will continue (Barnhart et al., 2016; Crawford et al., 2021). Therefore, the continued monitoring

of sea ice conditions and variability are critical for understanding the coupled ocean-sea-atmosphere (OSA) system.

Active microwave remote sensing has proven to be an effective technology for sea ice monitoring in the Arctic due to its 24-h high-resolution imaging capability under all-weather conditions. Spaceborne synthetic aperture radar (SAR) systems, operating at a wide range of frequencies, have demonstrated their utility to detect and characterize sea ice dynamic and thermo-dynamic changes (Tucker et al., 1992; Cavalieri, 1994; Barber et al., 1995; Yackel and Barber, 2000; Kwok et al., 1998; Scharien et al., 2010; Ochilov and Clausi, 2012; Mahmud et al., 2016; Howell et al., 2018; Murashkin et al., 2018). C-band SAR satellites, such as ERS-1/2, ENVISAT-ASAR, RADARSAT-1/2,

* Corresponding author at: University of Calgary, Calgary, AB, Canada.

E-mail address: msmahmud@ucalgary.ca (M.S. Mahmud).

<https://doi.org/10.1016/j.rse.2022.113129>

Received 3 August 2021; Received in revised form 4 June 2022; Accepted 10 June 2022

Available online 28 June 2022

0034-4257/Crown Copyright © 2022 Published by Elsevier Inc.

(<http://creativecommons.org/licenses/by-nc-nd/4.0/>).

This is an open access article under the CC BY-NC-ND license

Sentinel 1A/B have been used extensively for operational Arctic sea ice monitoring. The choice of C-band as a preferred frequency was established in the late 1980s when thick and old MYI dominated the Arctic sea ice. However, in the new Arctic regime, thinner and younger sea ice has become the dominant ice type. As a result, recent studies have demonstrated L-band SAR imagery with its longer wavelength provides more robust estimates of Arctic sea ice over the annual cycle compared to C-band. For example, Casey et al. (2016) demonstrated improved sea ice separability between early to advanced melt seasons, using L-band SAR, compared to C-band. Mahmud et al. (2020) found more robust microwave backscatter signatures during melt onset and break-up for FYI at L-band compared to C-band. However, sea ice signatures during freeze-up were contaminated since the floes were mobile after break-up and the algorithm did not track individual floes, which warrants detailed detail investigation of new ice signatures from SAR frequencies. Howell et al. (2018) compared sea ice motion from C- and L-band SAR imagery and found L-band provided more sea ice motion vectors. L-band SAR also showed utility in characterizing sea ice roughness characterization during winter and melt seasons (Cafarella et al., 2019; Dierking and Dall, 2008; Johansson et al., 2017 and 2018). Given the existing (e.g., ALOS-2, SAOCOM), forth-coming (e.g., NISAR) and approved (e.g., ROSE-L) L-band SAR missions, there is a growing shift towards using L-band SAR for sea ice monitoring in the new Arctic. While previous studies have shown L-band SAR's ability to provide more robust estimates of Arctic sea ice, the freeze-up period, when the ice begins to grow, has received less attention. The thickness of sea ice influences heat exchange, especially when sea ice is thin (Maykut, 1982). Therefore, monitoring the formation and distribution of early-stage sea ice is critical for small to large-scale heat exchange estimates and for identifying frost flowers on new ice, which affect air/ice CO₂ exchange (Else et al., 2007) among other chemical and biological processes. Numerous studies have demonstrated that early-stage sea ice is better detected at L-band than C-band because of its greater penetration depth and reduced sensitivity to small-scale roughness (Arkett et al., 2008; Dierking and Busche, 2006; Johansson et al., 2018; Toyota et al., 2020).

Arctic sea ice classification has always been an active research area, given the complexity and variability of sea ice type distribution and thickness. Zakhvatkina et al. (2019) provided an overview of SAR data-based methods to identify sea ice classes. While a limited number of studies used machine learning approaches, the majority of these studies focused on lead, ice and open water (OW) identification only by using dual- and fully-polarimetric C- and X-band SAR datasets (Geldsetzer and Yackel, 2009; Keller et al., 2020; Liu et al., 2015; Ressel et al., 2015, 2016). Aldenhoff et al. (2018) demonstrated the utility of a Neural Network (NN) classifier using C- and L-band dual-polarimetric SAR and one grey level co-occurrence matrix (GLCM) texture parameter to separate ice-class from OW. This study also showcased the superiority of L-band SAR to identify calm water/thin ice compared to C-band. However, identifying new ice within regions of young or FYI is more complex (Dierking, 2010). Singha et al. (2018) demonstrated Arctic sea ice classification performance using fully-polarimetric multi-frequency SAR. They reported that L-band SAR imagery could better discriminate between new ice and older types. However, an integrated approach combining L- and C-band SAR signatures, GLCM texture parameters and a machine learning approach has not been explored to identify newly formed ice classes during sea ice freeze-up.

This paper is outlined as follows. First, we investigate and analyze SAR signatures of open water, newly-formed Arctic sea ice with varied thickness classes. Next, we discuss the variability in C- and L-band SAR signatures. Then, we investigate and discuss the GLCM texture parameters derived from C- and L-band SAR imagery for each ice class. We also use a machine-learning algorithm to classify C- and L-band SAR imagery to identify ice classes and open water in two different regions. Finally, we analyze the classification performance.

2. Study area and data

2.1. Study area

This study examined two regions in the Canadian Arctic to capture a variety of sea ice conditions. First, we investigated the North Water Polynya (NOW) region between Greenland and Ellesmere Island (Fig. 1). The NOW polynya is a region of dynamic ice movement throughout much of the year and is formed and maintained through a combination of latent and sensible heat mechanisms (Barber et al., 2001). This region experiences a southward flow of water and sea ice from the Arctic ocean (Melling et al., 2001; Moore et al., 2021). Locally formed new and young ice types can be closely associated with imported thicker and older ice (Mundy and Barber, 2001). During freeze-up, the NOW region is extensively covered by open water areas; however, it becomes predominantly ice-covered by the end of the fall season (Mundy and Barber, 2001). Open water is dominant on the eastern coast, whereas ice concentration is higher on the west coast due to coastal downwelling and southward ice and ocean velocities (Melling et al., 2001; Moore et al., 2021).

We also investigated the Victoria Strait (VS) region in the southern part of the Canadian Arctic Archipelago (CAA) (Fig. 1). Sea ice in this region is typically landfast from November to July. Both MYI and a variety of FYI classes are found in this region. MYI found in this region is formed locally via FYI aging and advected from north (Melling, 2002; Howell et al., 2008). As a result, MYI in this region often contains a mix of MYI that has survived several melt seasons and ablated and broken up while in transit moving southward through the CAA. Therefore, the MYI found in Victoria Strait is more deteriorated than the MYI found in the NOW region.

2.2. Data

2.2.1. Synthetic aperture radar (SAR)

We used two pairs of SAR imagery in this study. For the first pair, C- and L-band ScanSAR imagery were acquired from dual-polarized (HH + HV) RADARSAT-2 and Advanced Land Observation Satellite (ALOS)-2 PALSAR-2 sensors (hereafter, referred to as ALOS-2), respectively. Imagery from both sensors was acquired on December 19, 2016 over NOW (Fig. 1c). The time difference between acquisitions is 3 h and 23 min. The center frequencies for RADARSAT-2 are 5.405 GHz and 1.2 GHz for ALOS-2. ScanSAR imagery from RADARSAT-2 has a pixel spacing of 50 m covering a 500 × 500 km² area. The incidence angle varies from 20 to 49° from near to far range. RADARSAT-2 data can be ordered from Natural Resources Canada (<https://www.eodms-sgdot.nrcan-rncan.gc.ca/>). ScanSAR imagery from ALOS-2 has a pixel spacing of 25 m and covers 350 × 355 km² area, and incidence angle ranges from 26 to 49°. Both the scenes consist of HH and HV bands. However, the HV band in the ALOS-2 scene had azimuth scalloping; therefore, we use only the HH channel for analysis. ALOS-2 data can be ordered from <https://alos-pasco.com/>.

For the second pair, we used HH-polarized ScanSAR C-band and L-band SAR imagery over VS on November 1, 2009, acquired from RADARSAT-2 and ALOS PALSAR (hereafter, referred to as PALSAR) sensors (Fig. 1b). In ScanSAR mode, PALSAR acquires data at 100 m pixel spacing covering a similar area as PLASAR-2. The center frequency for PALSAR is 1.27 GHz. The image acquisition time difference was 4 h 27 min for the second pair. PALSAR dataset was acquired from Alaska Satellite Facility Distributed Active Archive Centers (<https://asf.alaska.edu/>).

2.2.2. Canadian Ice Service Digital Archive (CISDA)

We used the Canadian Ice Service Digital Archive (CISDA) to obtain ice type information in the NOW and VS regions on December 19, 2016, and November 2, 2009, respectively (Fig. 1). CISDA is a collection of daily and weekly ice charts prepared by the Canadian Ice Service (CIS)

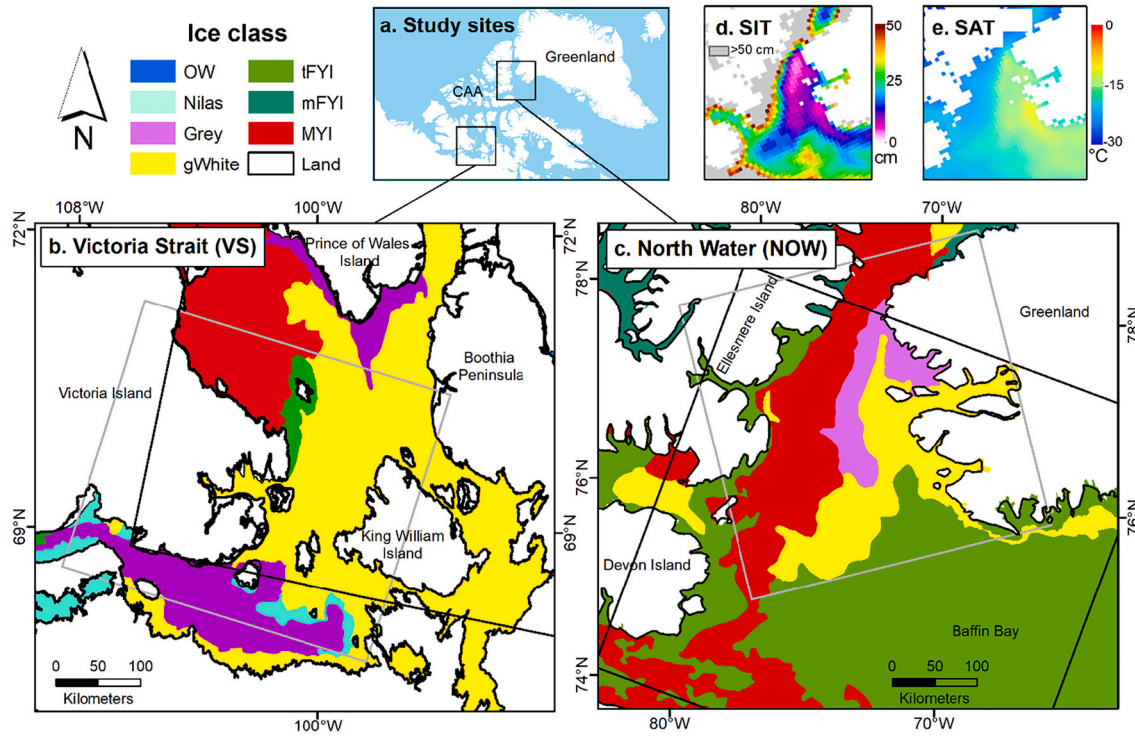


Fig. 1. Study sites are shown in an inset map (a). Victoria Strait (VS) and North Water (NOW) Polynya are shown in (b) and (c), respectively. The color-coded polygons in (b) and (c) denote different major ice types based on the Canadian Ice Service weekly ice chart on November 2, 2009, and December 19, 2016, respectively. For example, grey, gWhite, mFYI, tFYI, and MYI refer to grey ice, grey-white ice, medium first-year ice, thin first-year ice, and multiyear ice. The grey and black rectangles on (b) and (c) show the extent of L-band and C-band SAR imagery, respectively. SMOS-derived sea ice thickness (SIT) and surface air temperature (SAT) from NCEP reanalysis are shown in (d) and (e) for NOW only since data is not available for VS. The land areas are masked and shown as white.

since 1968. A variety of sea ice information acquired from satellite-based monitoring, ship-based observation, and operational models are used to prepare the ice chart. Ice chart provides information on-ice development, total concentration, partial concentration, and floe size distribution. These charts are available at <https://iceweb1.cis.ec.gc.ca/>. A detailed description of the CIS ice chart is provided by Tivy et al. (2011).

2.2.3. Soil Moisture and Ocean Salinity (SMOS)

The Soil Moisture and Ocean Salinity (SMOS) is a spaceborne L-band (1.4 GHz) radiometer capable of retrieving sea ice thickness (SIT) (Kaleschke et al., 2012; Tian-Kunze et al., 2014).

We used the SMOS-derived SIT and surface air temperature (SAT) from NCEP reanalysis (included as an auxiliary data in the SMOS product) of the NOW region acquired on December 19, 2016, to only aid our ice-class selection process (Fig. 1d and e). The maximum retrievable SIT from SMOS is 50 cm, making it an independent validation dataset for SIT during freeze-up (Kaleschke et al., 2012). SMOS provides daily coverage of the polar region at 35 km × 35 km resolution. Derived SMOS products can be downloaded freely from <https://data.seaiceportal.de/> (Grosfeld et al., 2016).

3. Methods

3.1. SAR image processing

C- and L-band imagery were obtained in level-1 and level-1.5 formats. After calibrating the SAR scenes, HH-polarized intensity images were converted into sigma naught backscatter coefficient (σ_{HH}^0 in dB). At level-1.5, ALOS-2 images were already converted from slant range to ground range and ellipsoid corrected upon data delivery. To maintain consistency between the SAR images, we geo-registered and projected to WGS84 Canada Polar Stereographic (ESPG: 5937). No speckle filter was

applied since the speckle effect was considered minimal on mean σ_{HH}^0 when a homogeneous region of interest was used to aggregate the data (Ulaby et al., 1981). ScanSAR imagery had reduced speckle through multi-looking and resampling. The image pair had different orbit directions, with descending orbit for RADARSAT-2 and ascending orbit for ALOS-2. To reduce the incidence angle induced variation in σ_{HH}^0 , we applied a frequency-specific incidence angle normalization technique on both image pairs, developed by Mahmud et al. (2018). We used a linear scaling of -0.22 dB/1° for C-band and -0.21 dB/1° for L-band scenes to normalize the scenes to 35° . Also, we resampled the ALOS-2 scene over NOW to 50 m using the bilinear sampling technique, leading to consistent pixel spacing with RADARSAT-2. For VS image pair, we resampled the RADARSAT-2 scene to 100 m leading to consistent 100 m pixel spacing with the PALSAR image.

3.2. Ice class selection

We used CIS ice charts to characterize sea ice types and distribution in the study areas. First, we extracted σ_{HH}^0 from ice chart polygons at both C- and L-band but found that σ_{HH}^0 statistics from each polygon were similar to each other. This is because CIS ice chart polygons are not homogeneous and contain different ice classes, resulting from placement limitations on the number of egg codes used on the ice chart by CIS. Therefore, we only discuss σ_{HH}^0 statistics from selected sites as identified in Figs. 2 and 3. For NOW, the ice chart on December 19, 2016, revealed five different ice types in the region, namely: nilas, grey, grey-white (gWhite), thin first-year ice (tFYI), medium first-year ice (mFYI) and multiyear ice (MYI) (Fig. 1c). We visually inspected σ_{HH}^0 variability in RADARSAT-2 and ALOS-2 SAR scenes and corresponding ice charts. Since we do not have in-situ measurements of SIT, we used SMOS to understand SIT distribution in the NOW region (Fig. 1d). For example, we found variability in SAT at tFYI and mFYI locations (Fig. 1e) because thicker ice increasingly prevents heat exchange from the ocean to the

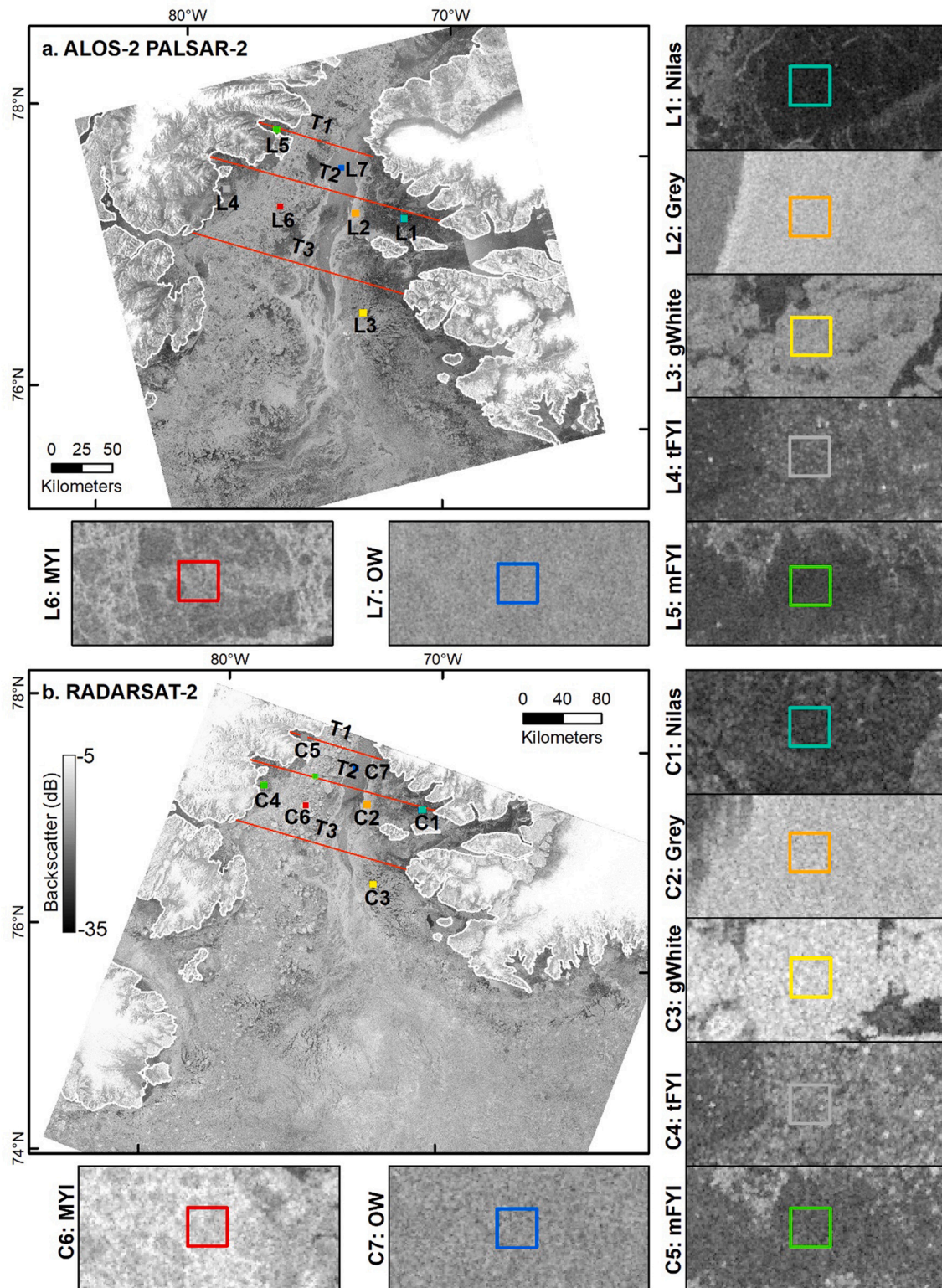


Fig. 2. The NOW region's L- and C-band imagery was acquired on December 19, 2016, from ALOS-2 (top) and RADARSAT-2 (bottom). The color-coded small boxes denote ROI from each ice type (e.g., nilas, grey, gWhite, tFYI, mFYI, MYI) and open water (OW). Each box is 1×1 km. The highlighted ROI areas are alpha-numerically coded (e.g., L1, C1). Transects lines (T1-T3) are shown in red, and land is outlined in white. (For interpretation of the references to color in this figure legend, the reader is referred to the web version of this article.)

atmosphere compared to thinner ice. The SMOS data also confirmed our interpretations from CIS ice analysts to finalize our selection of different ice classes. We also identified wind roughened open water areas in the SAR scenes. Similarly, the ice chart over VS denoted nilas, gWhite, tFYI

and MYI in the region on November 2, 2009 (Fig. 1b). Upon checking the time series of CIS ice charts in the VS region, we noticed that a few polygons in the region were prematurely identified as gWhite instead of grey, which was considered while selecting ROIs (Fig. 3). Finally, we

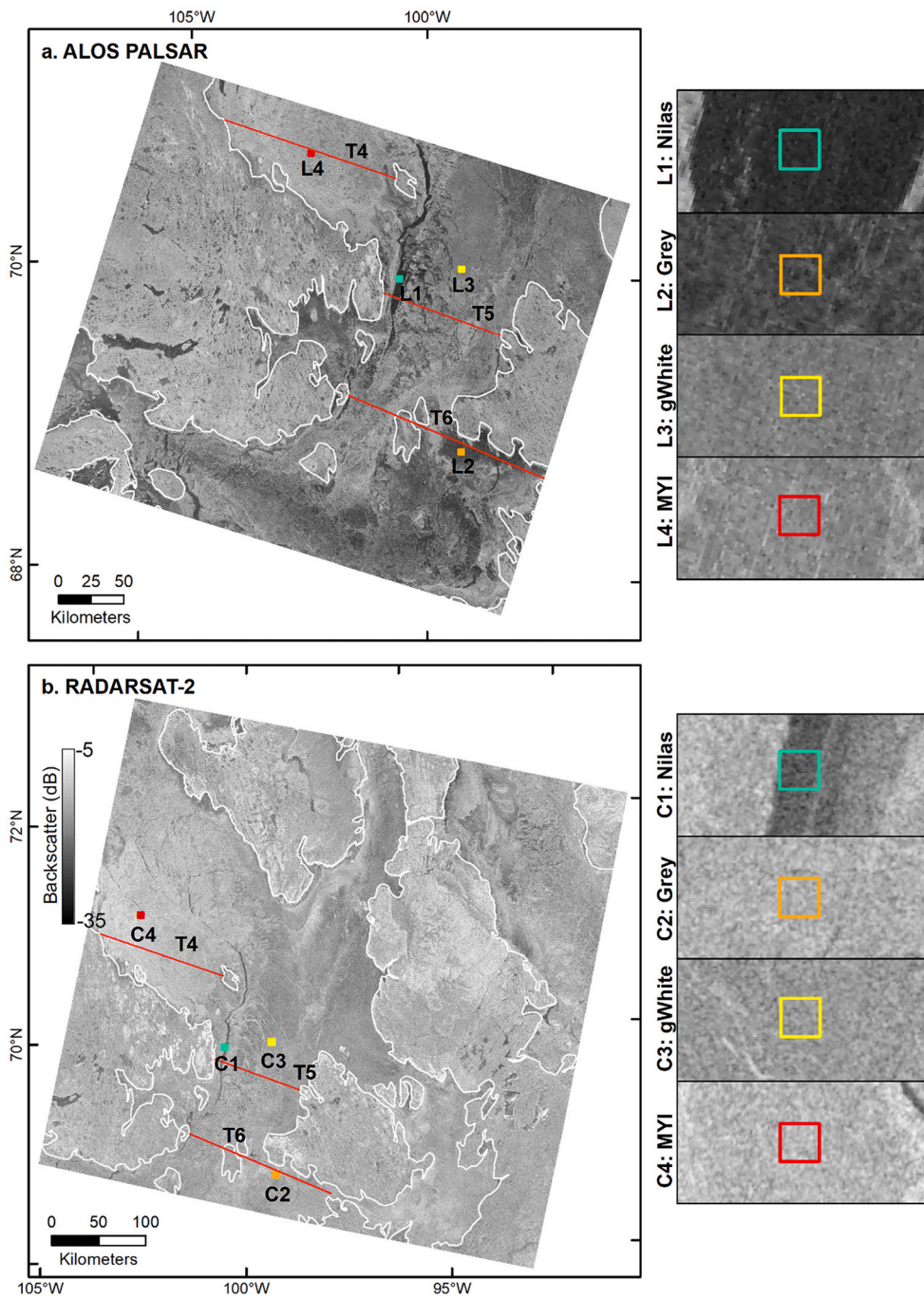


Fig. 3. The VS region's L- and C-band imagery was acquired on November 2, 2009, from ALOS PALSAR (top) and RADARSAT-2 (bottom). The color-coded small boxes denote ROI from each ice type (e.g., nilas, grey, gWhite, MYI). Each box is 1×1 km. The highlighted ROI areas are alpha-numerically coded (e.g., L1, C1). Transect lines (T4-T6) are shown in red, and land is outlined in white. (For interpretation of the references to color in this figure legend, the reader is referred to the web version of this article.)

selected nilas, grey, gWhite, tFYI, mFYI, MYI and open water for NOW, and nilas, grey, gWhite and MYI for VS for further analysis. A description of different ice classes is reported in Table 1.

We carefully selected a 1×1 km homogeneous region of interest (ROI) for each ice class. Each ROI (consisting of 100 pixels in VS and 400 pixels in NOW) was sufficient to derive necessary statistics and signatures for pixel-based analysis in the classification framework. After identifying ROIs for different ice classes on C-band scenes, we manually identified these locations in the L-band scenes considering the ice drift. The center of the ROIs was selected at least 3 km away from land to avoid any potential land contamination. We also assigned three transect lines over the sea ice area from west to east on the imagery to capture the variability of ice-class distribution in the region (Figs. 2 and 3). The transect lines (T1-T6) capture both homogeneous and mixed ice types in

Table 1
Ice terminology used in this study (adapted from Canadian ice Service).

Ice class	Thickness (in cm)	Characteristics
Nilas	< 10	Collective term for thin elastic-like newly formed ice types representing grease, light or dark Nilas.
Grey	10–15	Ice could be covered with moist and slushy snow.
Grey-White	15–30	Ice could be covered with frost flower or brine-wetted snow.
Thin FYI	30–70	Thin first-year ice with different roughness characteristics.
Medium FYI	70–120	Medium first-year ice.
MYI	>200	Second-year or older ice.

the regions to investigate the separability of the ice classes.

3.3. Grey-level co-occurrence matrix (GLCM)

The utility of grey-level co-occurrence matrix (GLCM) texture parameter has been proven to be a compelling probability statistic for image analysis and improved image classification accuracy in sea ice applications (Barber and Ledrew, 1991.; Clausi, 2002; Liu et al., 2015; Shokr, 1991). Using first- and second-order texture statistics, improved ice separability can be achieved from SAR image analysis. GLCM also shows a tabulation of how often a different combination of pixel intensities (a specific grey level) co-occur in an image or image section. The GLCM texture parameter calculations use the contents of GLCM to measure intensity variation at a given pixel. We calculated GLCM parameters by computing the joint probability density of a pair-wise combination of intensity values in a spatial window using displacement and orientation (Table 2). After a thorough review of Clausi (2002) and Scharien et al. (2017), we used 9×9 sliding windows at 64 grey-level quantization schemes at 4 inter-pixel distances by averaging all orientation angles. Six GLCM bands were created: Contrast (CON), Correlation (COR), Dissimilarity (DIS), Entropy (ENT), homogeneity (HOM), and angular second moment (ASM) (Table 2). The GLCM texture parameter was calculated from calibrated, log-scaled SAR scenes before applying incidence angle normalization. We did not apply any incidence angle normalization on new texture parameter bands since the incidence angle dependency value was negligible (Scharien and Nasonova, 2020) compared to the calculated textural parameter values and range found in this study. We also indicated overlapping coefficient (OVL) to discuss the GLCM texture area under two probability distribution functions simultaneously (Inman and Bradley Jr (1989). The higher OVL denotes a larger overlap in distribution, which leads to 'look-alike' signatures resulting in misclassification of ice classes.

3.4. New ice image classification and validation

SAR imagery is often the only information source available for operational sea ice monitoring. Based on the SAR data types (e.g., single-

, dual- or fully-polarimetric), several sea ice classification algorithms have been developed and operationally used to monitor Arctic sea ice, as summarized in Zakhvatkina et al. (2019). We used a support vector machine (SVM) algorithm for image classification. This machine-learning algorithm uses supervised learning models for image classification by modelling nonlinear decision boundaries through kernel functions (Vapnik et al., 1994). In addition to σ_{HH}^0 , we used GLCM parameters (Section 3.3) as a classification input to the SVM framework. The training datasets were built by visual inspection of the imagery (as outline in Section 3.2) with additional sites. With the σ_{HH}^0 and selected GLCM texture features as inputs, a decision tree was developed, and the SVM was implemented using a standard 'libsvm' library. We chose to use Radial Basis Function (RBF) as the kernel type along with 'gamma' (kernel parameter) value of 0.5 and 'cost' (penalty parameter) value of 10. For the RBF based kernel type the recommended range for 'gamma' value is in between 0.0001 and 10 and for the recommended value for 'cost' is in between 0.1 and 100. We used a grid search approach to tune these parameters. The initial training dataset were randomly divided into training (80%) and validation (20%) dataset and tuned the gamma value based on the resulting cross-validation accuracy. The value for 'gamma' and 'cost' remains same for all classified images. A detailed description of the classification algorithm can be found in Liu et al. (2015). We used open water (OW), nilas, grey, gWhite, FYI and MYI categories in the classification. Since the mFYI class covers <5% (by sea ice area) in the study region, we merged tFYI and mFYI types and considered them FYI in the classification scheme.

Next, we developed and applied a novel 'dual-frequency classifier' where both C- and L-band imagery were used. We used the same SVM classifier for the dual-frequency approach, which was embedded within rule-based decisions with conditional operators. Rule-based decisions were based on backscatter responses from different ice classes. First, we used the C-band image for NOW and applied the SVM algorithm to detect OW, MYI and 'other' classes. If a classified pixel falls under the 'other' class, the classifier runs the SVM with L-band imagery to assign a thinner ice class to that pixel. The decision to identify OW and MYI at the beginning from C-band was based on the distinct signature of OW and MYI to avoid confusion with 'other' ice classes. Given the similarity of C-band backscatter signatures for gWhite and MYI in VS, we updated the order of the rule-based decisions to improve our classification performance in VS. For example, we used L-band SAR at the beginning to identify gWhite and 'other' classes followed by C-band SAR to identify MYI from the 'other' pixels. Afterward, we used L-band to classify 'other' into nilas and grey ice classes. Finally, all classes were combined to produce the final classified map. We did not put C- and L-band imagery and associated GLCM texture parameters into SVM as combined parameter sets since each of them adds additional uncertainty to the individual ice class.

We used two techniques to validate the classification outputs. First, we identified OW and ice classes on three transect lines. Then, we segmented the transect lines based on dominant ice classes and showed major classes based on the total number of pixels on the transect segments. These ice classes are identified from visual inspection, as stated in Section 3.2. Similarly, we extracted ice classes from classified images and showed major ice classes to compare against the visual inspection supported by SMOS-derived SIT of the NOW region. Secondly, we assessed the classified images' accuracy and present class-based and overall accuracy. Although areas from each ice class are not equal, we selected 100 pixels from each ice class and OW to understand the classifier's performance using a single frequency approach (e.g., only C- or L-band) and a dual-frequency approach (both C- and L-band).

Table 2
Grey-level co-occurrence-based texture statistics equations.

Parameters	Derivation
Contrast (CON)	$\sum_{n=0}^{N_g-1} n^2 \left\{ \sum_{i=1}^{N_g} \sum_{j=1}^{N_g} p(i,j) i-j = n \right\}$
Correlation (COR)	$\frac{\sum_i \sum_j (ij) p(i,j) - \mu_x \mu_y}{\sigma_x \sigma_y}$
Dissimilarity (DIS)	$\sum_i \sum_j i-j p(i,j)$
Homogeneity (HOM)	$\frac{1}{\sum_i \sum_j 1 + (i-j)^2 p(i,j)}$
Angular Second Moment (ASM)	$\sum_i \sum_j \{p(i,j)\}^2$
Entropy (ENT)	$-\sum_i \sum_j p(i,j) \log(p(i,j))$

where N_g is the number of distinct grey levels in the quantized SAR image. The GLCM information is denoted by the matrix of relative frequencies $p(i,j)$ with two neighbour pixels, one with grey level i , while the other with grey level j . $p(i,j)$ is the (i,j) th entry in a normalized GLCM. μ_x , μ_y , σ_x , σ_y are the mean and standard deviations of the rows and columns of the image matrix. The GLCM equations are adopted from Haralick et al. (1973) and Soh and Tsatsoulis (1999).

4. Results and discussion

4.1. C- and L-band backscatter variability during the freeze-up period

Fig. 4 illustrates the variability in σ_{HH}^0 from both C- and L-band imagery for open water and ice classes. Nilas has the lowest σ_{HH}^0 at both L- and C-bands. σ_{HH}^0 for nilas is -30.1 ± 1.2 dB at L-band and -27.2 ± 1.6 dB at C-band for NOW, and -24.3 ± 2.3 dB at L-band and -24.01 ± 1.5 dB at C-band for VS. σ_{HH}^0 for nilas in NOW fall below the ALOS-2 noise floor of -26 dB (Kankaku et al., 2009) and close to RADARSAT-2 noise floor of -28 dB (Caves and Williams, 2015). The very low σ_{HH}^0 suggests specular scattering from a relatively smooth ice surface. Isleifson et al. (2010) reported similar σ_{HH}^0 from homogeneous nilas acquired from a ship-based C-band polarimetric radar in the Cape Bathurst polynya in the southeastern Beaufort Sea.

As the ice thickens, an increase in σ_{HH}^0 from grey to gWhite ice can be found at C-band. However, the opposite is true for L-band σ_{HH}^0 for both regions. In NOW, σ_{HH}^0 for grey is -16.8 ± 1.1 dB at L-band and -17.1 ± 1.8 dB at C-band, where a decrease of 2.1 dB is observed at L-band (i.e., -18.57 ± 1.3 dB), and an increase of 2.76 dB is observed at C-band for gWhite (i.e., -14.3 ± 1.7 dB). Similarly, in VS, σ_{HH}^0 for grey is -14.2 ± 1.6 dB at C-band, which is increased by 2.3 dB for gWhite (i.e., -16.5 ± 1.5 dB). At L-band, the 2.7 dB decrease in σ_{HH}^0 from grey (i.e., -16.38 ± 1.8 dB) to gWhite (i.e., -19.1 ± 1.9 dB) is similar to NOW region. The presence of brine-rich and radar-rough rime/frost flowers and/or brine-

wetted snow (due to snow brine wicking from frost flowers or ice surface) on gWhite ice may have caused enhanced surface scattering, resulting in a stronger C-band σ_{HH}^0 (Onstott, 1992; Isleifson et al., 2010, 2014; Nghiem et al., 1997). Although we do not have in-situ observations, small-scale roughness features such as frost flowers, with their associated high salinity lumps, and snow accumulation followed by brine wicking from frost flowers could have been a major distinctive surface characteristic difference between grey and gWhite ice (Onstott, 1992; Nghiem et al., 1997).

As the ice becomes thicker, a decrease in σ_{HH}^0 is found for tFYI and mFYI for both C- and L-band. L-band σ_{HH}^0 for tFYI and mFYI are -22.4 ± 1.7 dB and -26.3 ± 1.2 dB, respectively. With increasing FYI ice thickness, desalinization allows greater L-band penetration into the ice volume (Dierking and Dall, 2007), resulting in lower σ_{HH}^0 , likely due to increased loss. The standard deviation for tFYI is the highest at L-band compared to other ice classes. C-band σ_{HH}^0 for tFYI and mFYI become increasingly lower with thickness with σ_{HH}^0 of -18.5 ± 2.2 dB and -23.2 ± 1.5 dB, for tFYI and mFYI, respectively. The desalinization with increasing thickness may also allow increasing penetration of C-band causing it to decrease (Barber and Nghiem, 1999), again, likely due to increased loss. However, an accumulating snow cover may also develop at this stage, which can wick brine from the ice surface into the snow volume, creating a brine-wetted snow layer leading to enhanced absorption/scattering of C-band microwaves, reducing backscatter from the underlying ice surface (Onstott, 1992).

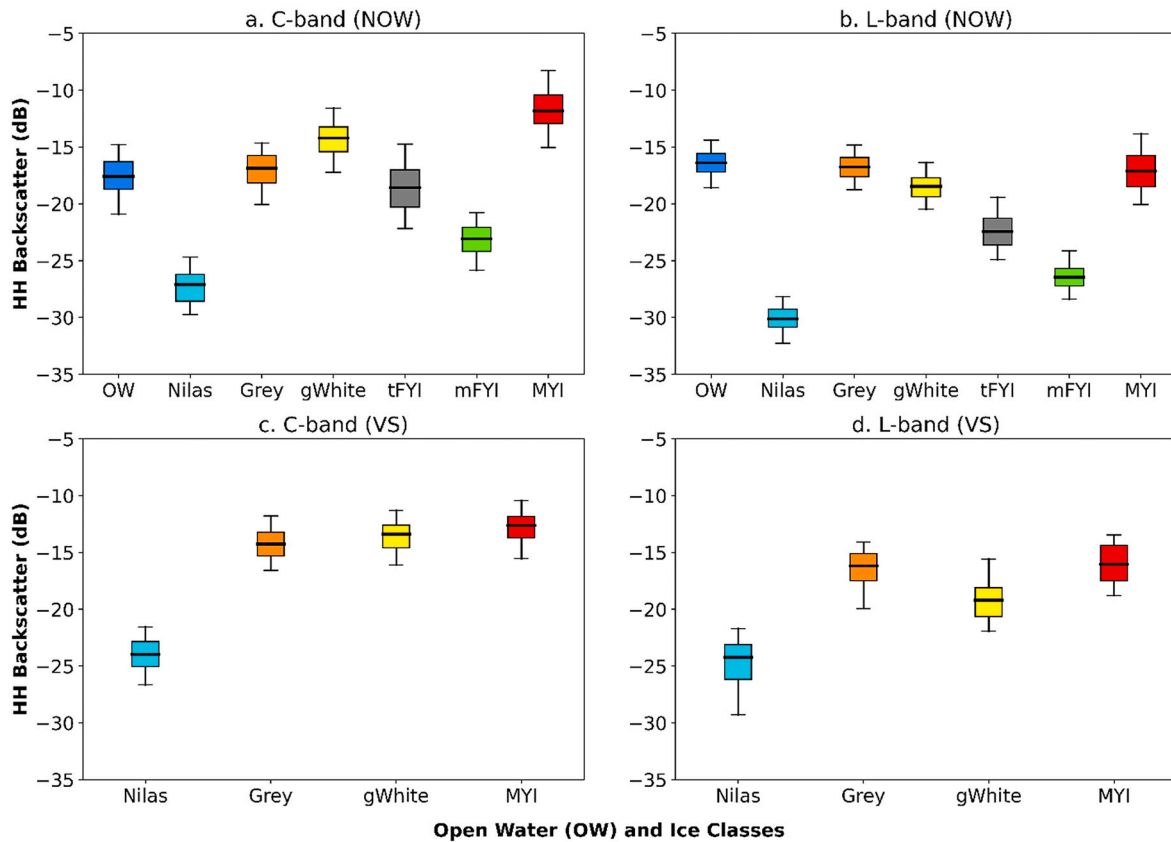


Fig. 4. Box plots of σ_{HH}^0 at both C- and L-band for open water (OW) and different ice types. The median lines are shown in black. The color-coded box plots correspond to the site locations in Figs. 2 and 3. For VS and NOW, each box plot consists of 100 and 400 pixels, respectively for each ice class.

For MYI, L-band σ_{HH}^0 is -17.1 ± 1.9 dB and -15.9 ± 1.8 dB in NOW and VS, respectively, that is similar to the young ice signatures (i.e., grey and gWhite). MYI is usually rougher than tFYI and mFYI; therefore, surface scattering for MYI will be higher than for tFYI and mFYI. Moreover, L-band penetrates deeper into the MYI structure due to its lower dielectrics at this frequency, contributing volume scattering and further increasing MYI σ_{HH}^0 compared to tFYI and mFYI (Dierking et al., 1999; Dierking and Dall, 2007). σ_{HH}^0 of -11.7 ± 1.9 dB and -12.7 ± 1.5 dB are found for MYI at C-band for NOW and VS, respectively, which is higher than other ice classes observed in this study. σ_{HH}^0 for MYI found in this study is typical for the Canadian Arctic as reported in previous studies at this time of the year (Howell et al., 2019; Mahmud et al., 2018 & 2016). At L- and C-band, surface scattering becomes increasingly dominant over volume scattering as the MYI ice surface roughness increases. Volume scattering is only dominant for C-band if a MYI surface is radar smooth (i.e., refrozen melt pond) (Kim et al., 1984), however, ice volume scattering contribution at L-band cannot be ruled out. A MYI surface appears smoother at L-band given its longer wavelength; therefore, surface scattering is higher for C-band. The upper layers of MYI contain entrapped air inclusions that are relatively small at L-band wavelengths, but larger at C-band wavelengths, adding additional volume scattering at C-band (Winebrenner et al., 1994). Therefore, MYI backscatter is generally lower for L-band compared to C-band, as seen in Fig. 4.

Based on this comparison, we can make the following deductions. First, although nilas shows very low σ_{HH}^0 , σ_{HH}^0 increases for grey in both C- and L-band with increasing SIT. While σ_{HH}^0 increases from grey to gWhite ice at C-band followed by a dip in tFYI, L-band shows a continuous decrease in σ_{HH}^0 from grey to mFYI with the increasing thickness (Fig. 4). The observable difference in C-band σ_{HH}^0 for grey and gWhite may indicate the presence of brine-rich frost flowers and/or saline snow that caused an increase in σ_{HH}^0 for gWhite ice as reported in previous studies (Isleifson et al., 2010, 2014; Nghiem et al., 1997; Onstott, 1992). σ_{HH}^0 continuously decreases as microwave signal at L-band penetrates more into the ice volume. If frost-flowers are indeed present, surface roughness should have minimal impact on σ_{HH}^0 at L-band, in contrast to C-band.

Secondly, the variability of σ_{HH}^0 (i.e., standard deviation) is higher in C-band than L-band for all ice types in the NOW region. The opposite is true for L-band since sea ice roughness features are more dominant in VS (Cafarella et al. (2019)). At C-band, a distinct increase in σ_{HH}^0 is found for MYI, which is higher by 2.6 dB compared to other ice types; however, at L-band, σ_{HH}^0 for MYI falls within the range of Grey and gWhite ice (Fig. 4). Furthermore, the highest variability in C-band σ_{HH}^0 is found for tFYI and MYI compared to other ice types. Owing to its longer wavelength, L-band exhibits lower σ_{HH}^0 for MYI compared to C-band, mainly due to its reduced microwave interactions with small-scale roughness, air bubbles and brine inclusions within the ice volume (Dierking and Dall, 2007; Winebrenner et al., 1994). The σ_{HH}^0 for OW is only representative of the wind conditions present at each satellite acquisition time, and can therefore not be generalized since OW's true range of C- and L-band backscatter is much larger.

4.2. Sea ice GLCM textural parameter characteristics

Six co-occurrence texture parameters are investigated to understand GLCM statistics of different ice types and aid SVM classification (please see the Introduction of how the six GLCM parameters are chosen). These parameters explain the different pixel-to-pixel relationships for different parts of the images representing different ice types. Given the similarity

of the distribution in both regions, we only show the distribution of σ_{HH}^0 and selected GLCM texture parameters for NOW in Fig. 5.

For Contrast (CON), L-band shows lower values for most classes than C-band, which means more intensity contrast among each class is found at C-band than L-band. For grey, both the frequencies show similar distributions. All classes show leptokurtic distributions at L-band, with most values concentrated near the mean. For nilas and grey, we find significantly lower values. Grey ice is more separable from other new ice classes at CON; however, it overlaps with MYI (OVL is 0.67). MYI shows the highest CON value among all classes, which indicates that MYI pixels are more diverse in intensity. At C-band, nilas, grey, gWhite and mFYI exhibit normal distributions, tFYI a platykurtic distribution, and MYI show a positively skewed distribution.

Similarly, C-band shows greater dissimilarity (DIS) for all classes than L-band, which means a larger dissimilarity (or linear contrast) among similar pixels within the ice classes. All classes show leptokurtic distributions at L-band, and only gWhite and OW show leptokurtic distribution at C-band. While mFYI shows the lowest DIS value at C-band, OW shows the lowest value at L-band. Most of the classes overlap at C-band, except for tFYI, which is separable from other classes (OVL for MYI and mFYI is 0.34). At L-band, ice classes are overlapped in two groups (e.g., tFYI and MYI in one group, and Nilas, grey, gWhite, OW, mFYI in another group).

For entropy (ENT), Nilas shows the lowest, and tFYI shows the highest value at C-band. Although most classes show leptokurtic distributions at C-band, they overlap each other (e.g., OVL for grey and gWhite is 0.87). ENT is lower at L-band than C-band, meaning within class pixels are more random at C-band than L-band. Looking at separability, it can be noticed that two groups of classes overlap each other at L-band where tFYI and MYI are in a group. Distribution of gWhite has the highest kurtosis at L-band, where OW shows the highest kurtosis at C-band.

In contrast to other texture parameters, homogeneity (HOM) at C-band is lower than L-band. A wider distribution of HOM is found at both frequencies for each class, and most classes have overlapping HOM at both C- and L-band. For example, OVL for grey and gWhite is 0.67 and 0.73 at C- and L-band, respectively.

GLCM texture parameters show diversified distributions for some ice classes at both C- and L-band, which can be useful for classification, where ice-class separability plays a critical role in classification performance. For example, ENT could separate thicker ice classes at L-band, where DIS shows better separability for thicker ice at C-band. This information will likely aid the classification algorithm to maximize the performance. Additionally, we looked at the correlation coefficients between σ_{HH}^0 and GLCM texture parameters (not shown). The correlation coefficient is statistically significant, however, not strong (<0.4). We couldn't compare these relationships with previous studies (Scharien and Nasonova, 2020; Shokr, 1991), since they focused on winter sea ice conditions.

4.3. Sea ice classification

SVM classification results for the C-band and L-band SAR imagery are presented in Figs. 6-9, which are based on variability in σ_{HH}^0 and six GLCM texture parameters. Additionally, we used both C- and L-band imagery as input to the classifier and resulted from the dual-frequency classifier are presented in Figs. 10 and 11.

At C-band, nilas and gWhite ice types dominate NOW (Fig. 6a), and MYI and grey are the dominant ice classes in VS (Fig. 7a). OW is well detected in NOW by the SVM algorithm mainly due to its unique

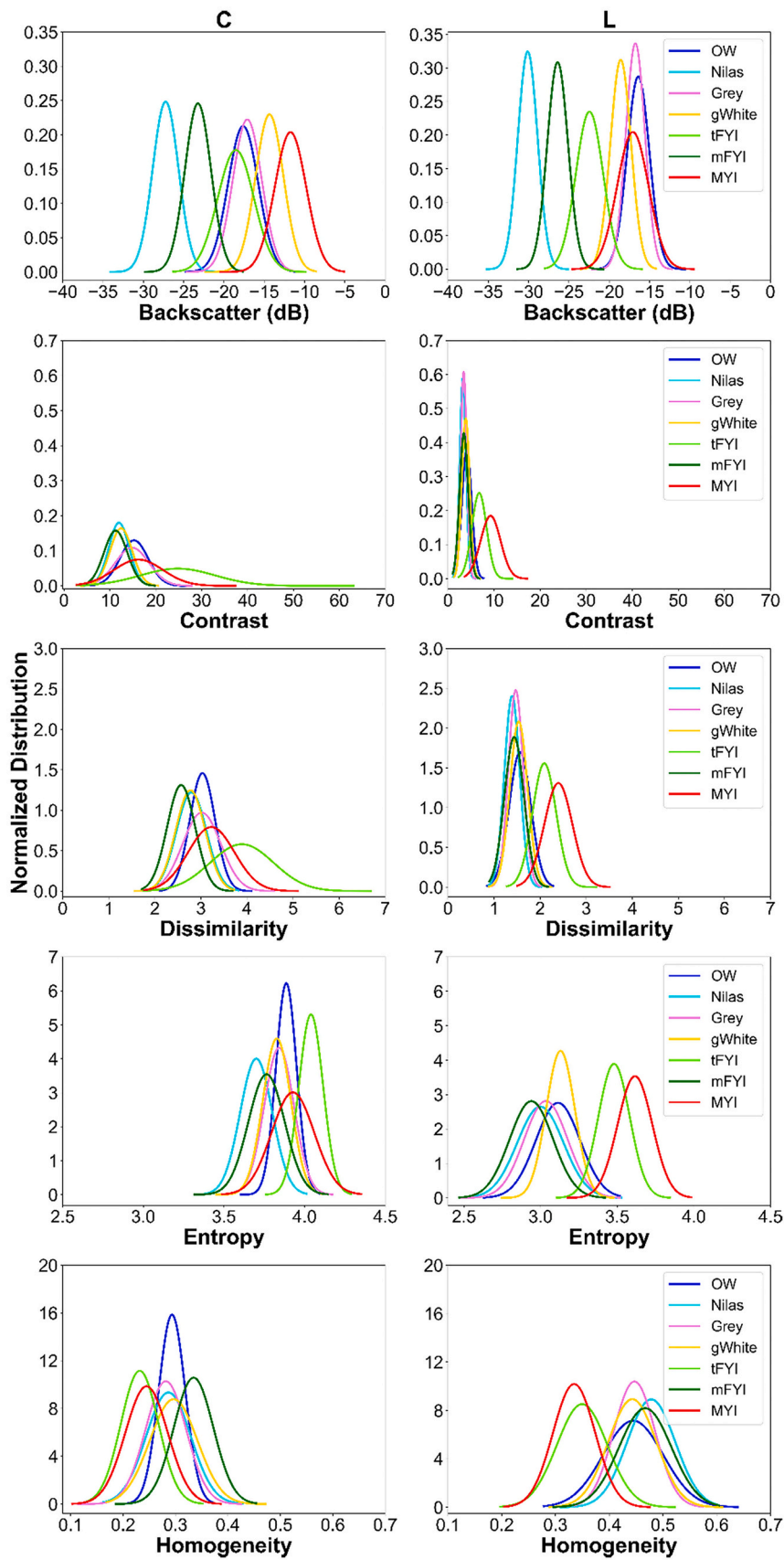


Fig. 5. Distribution of σ_{HH}^0 and selected GLCM texture parameters for different ice types in NOW. The texture statistics are based on ROIs that contain 100 and 400 pixels for VS and NOW, respectively.

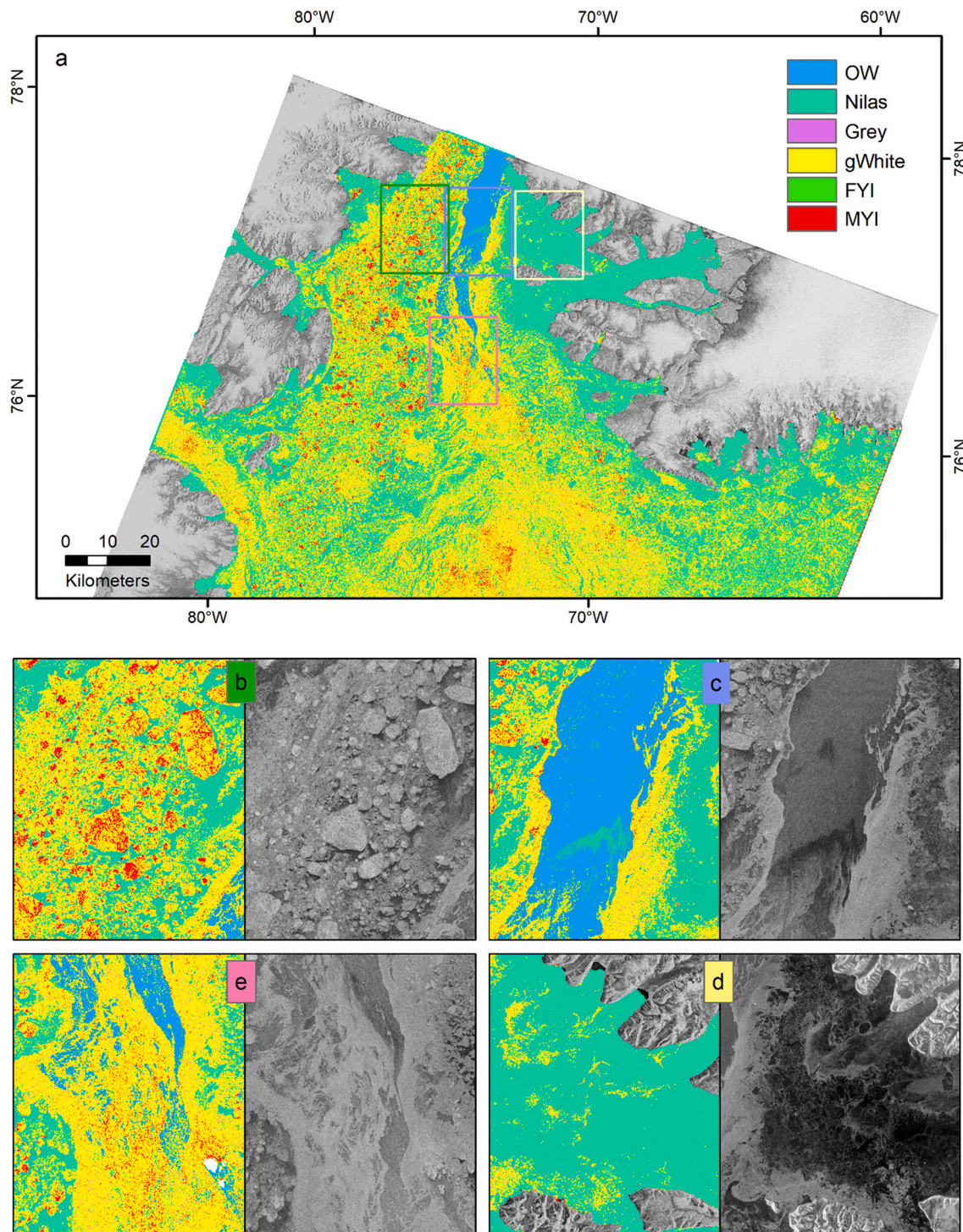


Fig. 6. Color coded-classified image from C-band SAR in North Water (NOW) is shown in (a). To demonstrate classification performance in different regions, highlighted areas are shown in b-e. Calibrated SAR scene are shown in the background (a), and beside highlighted areas (b-e).

response in σ_{HH}^0 . Of course, OW classification is limited to its wind conditions at acquisition; further study is needed to evaluate the ability of the SVM algorithm to classify OW at other wind speeds and directions. While grey and gWhite are found sparsely in the SAR scenes, a very small amount of FYI is identified in NOW. In VS, grey is misclassified as gWhite and MYI (Fig. 7c). Figs. 6b and 7d are occupied mainly with MYI floes, where large floes are identified well in NOW; however, smaller floes are mixed with gWhite in both regions. Notably, grey ice located in the bottom part of the VS imagery is misclassified as a mixture of gWhite

and MYI due to the 'look-alike' signature of these ice classes, as shown in Fig. 4. MYI is misclassified as gWhite and grey in NOW and VS, respectively, due to the closeness of backscatter and GLCM signatures at the C-band for these classes. New ice areas between MYI floes are well identified in the classified image in both regions. Fig. 6b and 7e shows that grey ice is mixed with gWhite and MYI, respectively. Wind-roughened OW is identified as expected with new ice in the middle of the OW region (Fig. 6c). A region dominated with gWhite ice is shown in Fig. 6e, where gWhite is the dominant ice class in the classified image.

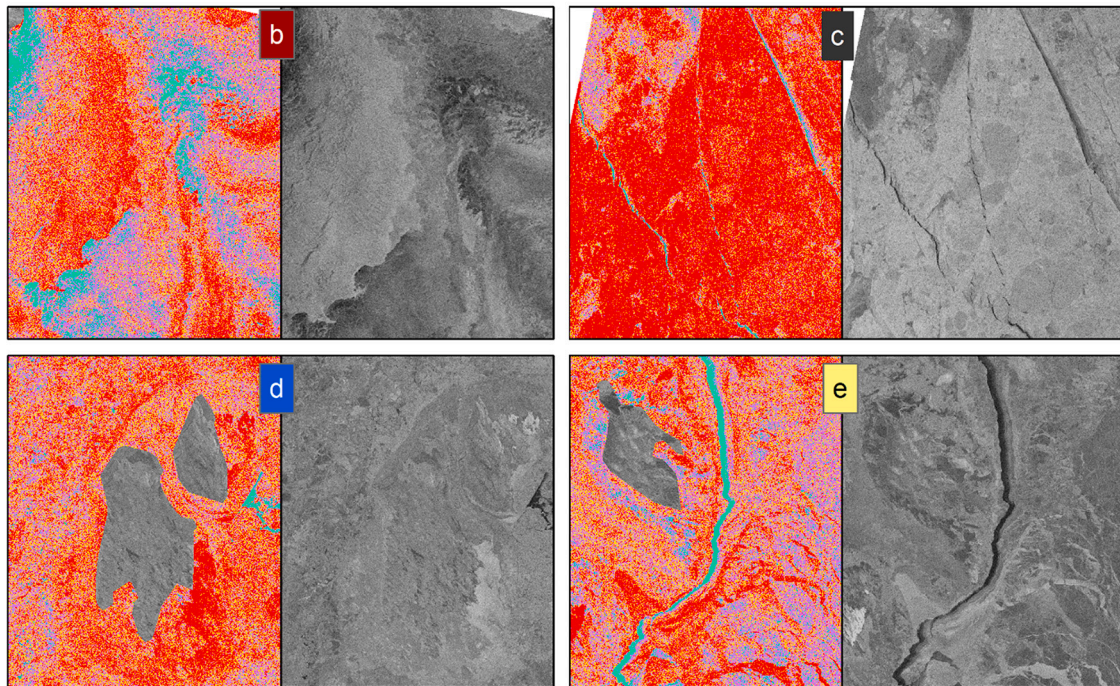
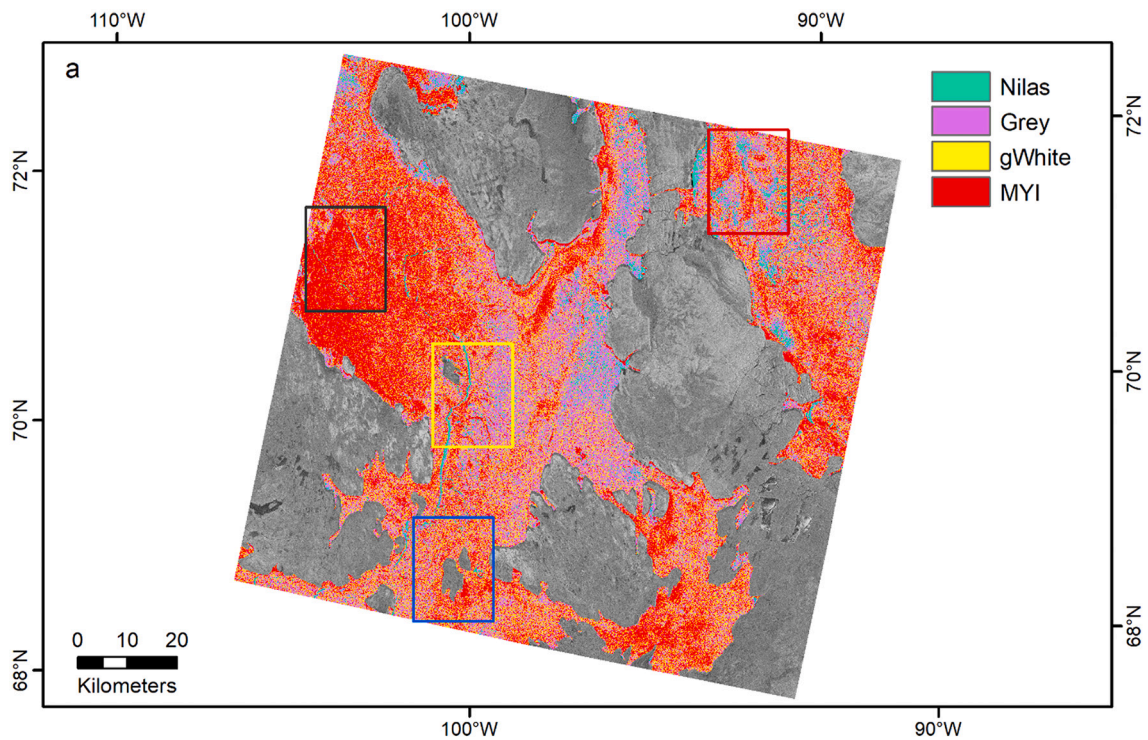


Fig. 7. Same as Fig. 6, but for C-band in Victoria Strait (VS).

However, many gWhite pixels are classified as MYI due to their smaller separability. Close to the land, nilas in NOW is identified in the classified image as found in visual inspection. However, it seems like the nilas class is over-estimated where gWhite and FYI are classified as nilas. Similar misclassification is also located in the north-western part of the image where the only mFYI (shows as FYI in classification) is found, leading to the ice being classified as nilas. Similarity in σ_{HH}^0 and GLCM texture parameters result in misclassification of these two ice types. Since we do not have any FYI in VS, nilas is detected in an elongated

pattern as expected in the C-band image (Fig. 6e).

Nilas and grey are reasonably identified at L-band in the classified imagery, except for MYI, which is over-estimated in NOW (Fig. 8a) and under-estimated in VS (Fig. 9a). Fig. 8b shows sea ice areas dominated by gWhite and MYI, where large MYI floes are reasonably-identified; however, many gWhite areas are misclassified as MYI, which results in MYI over-estimation. Smaller nilas areas within the MYI floes are also identified (Fig. 8e). The classifier could not differentiate well between MYI, grey and gWhite at L-band mainly due to the similar response in

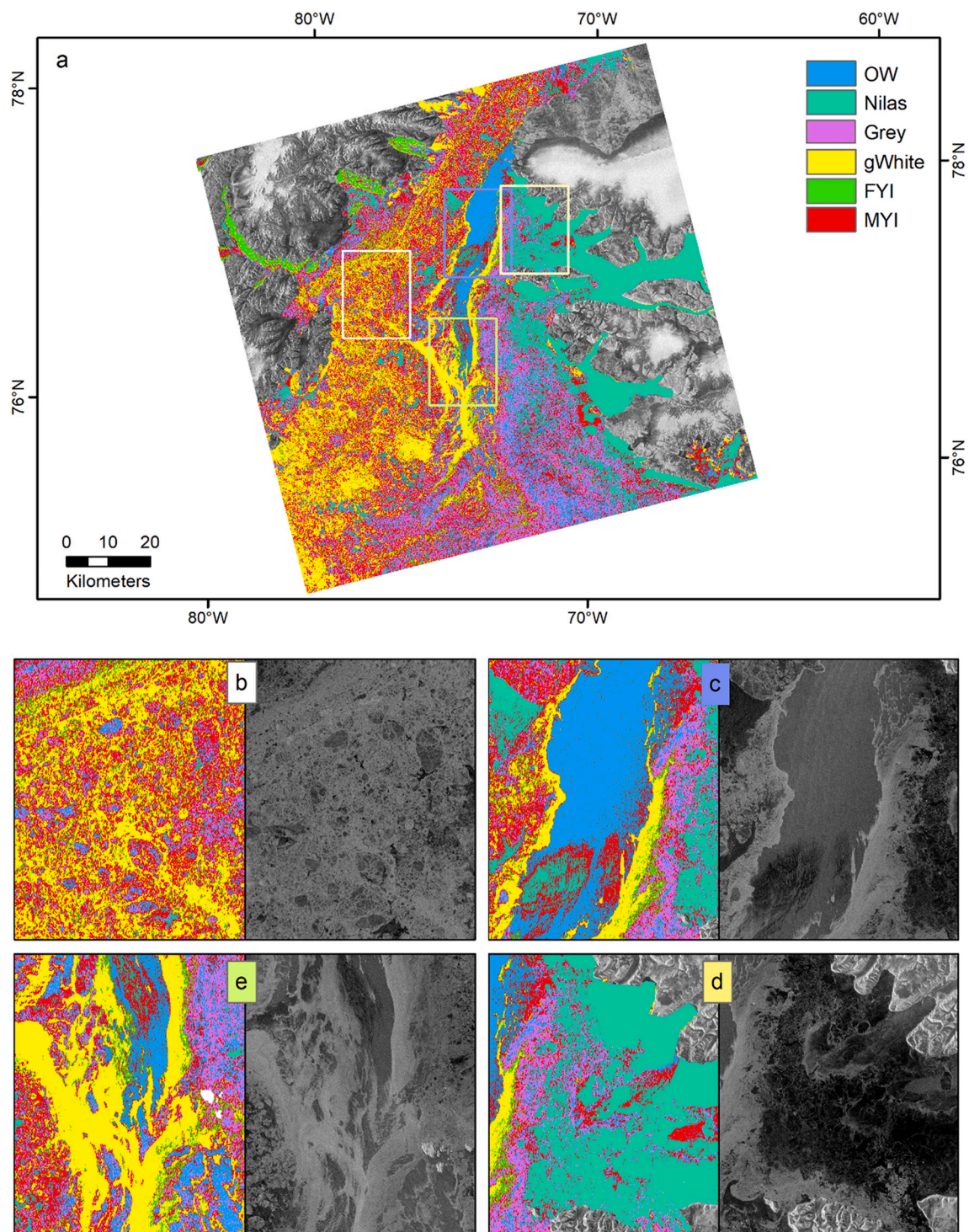


Fig. 8. Same as Fig. 6, but for L-band in the North Water (NOW) region.

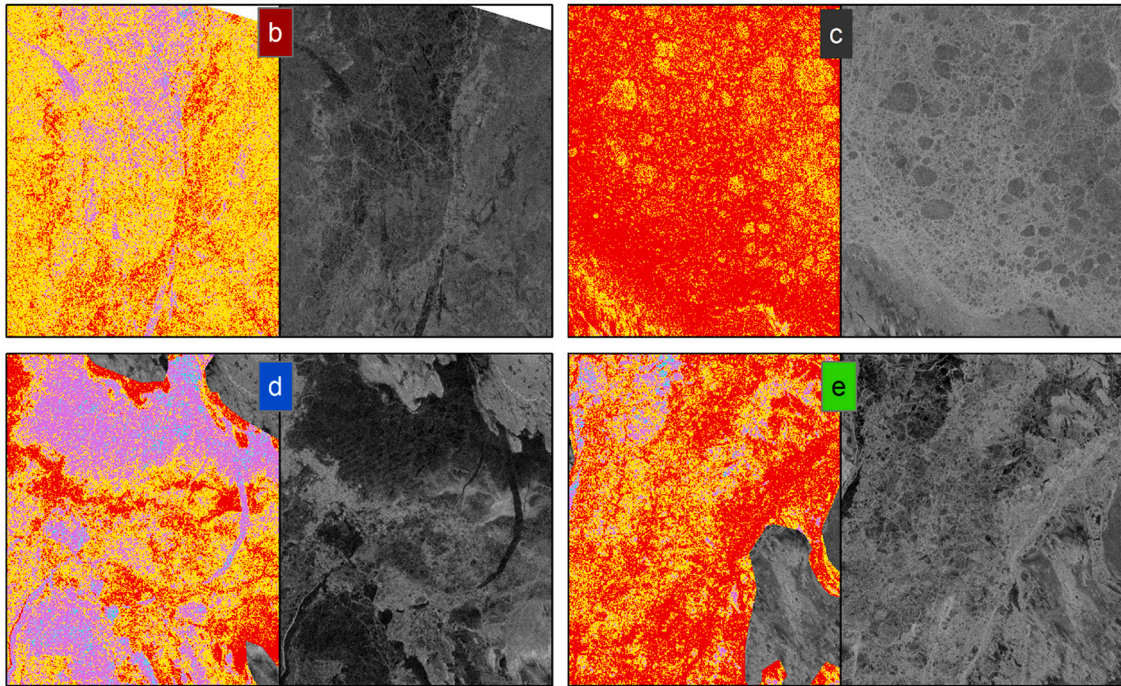
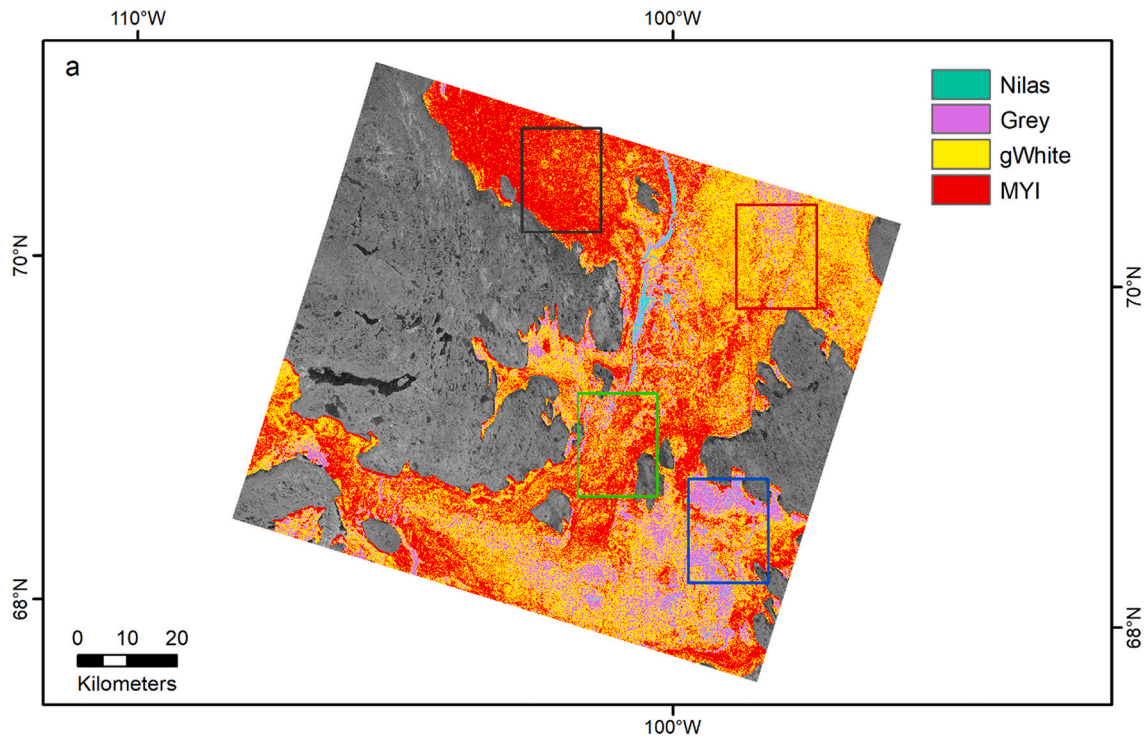


Fig. 9. Same as Fig. 6, but for L-band in the Victoria Strait (VS) region.

σ_{HH}^0 and GLCM texture parameters in both regions as shown in Figs. 4 and 5. Areas with OW are well classified with nilas within (Fig. 8c). However, OW area with a high wind causes higher σ_{HH}^0 are classified as MYI. Grey ice is captured well in addition to gWhite and nilas ice (Figs. 8e and 9d). Coastal areas are reasonably classified for nilas, grey and gWhite ice; however, a significantly smaller region is classified as MYI, which belongs to the gWhite ice-class (Fig. 8d). Overall, thinner ice classes are classified as expected. L-band identifies all classes in a region mixed with various ice classes (Figs. 8e and 9d). Although nilas, grey and FYI are appropriately identified, many gWhite areas are classified as

MYI (Fig. 8b) and vice versa (Fig. 9e).

Overall, we found contrasting performance in identifying ice classes using the SVM classifier. At C-band, MYI floes in NOW are well identified with minimal conflict with other ice classes; however, an opposite result is found at L-band, where MYI is largely misclassified as gWhite and vice versa. However, in VS, grey, gWhite and MYI signatures at C-band are very close to each other. However, L-band shows improved identification of nilas, grey and gWhite compared to C-band. Improved OW in NOW identification is found at C-band compared to L-band, also reported in Dabboor et al. (2017). Therefore, we use C- and L-band by

using C-band to identify OW and MYI and L-band to identify other thinner ice classes. Initially, we applied the same order of rule-based decisions in VS, similar to NOW. The classifier underperformed, where MYI was substantially over-estimated from grey and gWhite classes due to 'look-alike' backscatter and GLCM texture signatures (not shown). Therefore, we used a slightly different order of rule-based decisions in a dual-frequency classifier for VS (see Section 3.4) and found improved classification performance in VS. We also applied the modified algorithm in NOW; however, we did not find any significant improvement in classification performance (not shown).

Figs. 10 and 11 show results from the dual-frequency classifier, and it

is visually apparent the classification results improved substantially compared to the single frequency classifiers. For instance, OW is well defined with minimal misclassification compared to Figs. 6 and 7. MYI floes are well defined, which substantially improves C-band classification. Previously, MYI areas were mixed with gWhite in the C-band classification (Figs. 6 and 7) and extensive gWhite areas were classified as MYI at L-band (Figs. 8 and 9). gWhite is classified as expected with minimal misclassification with MYI. Grey ice areas are identified correctly among gWhite and Nilas ice areas. Looking closely at more complex sea ice areas (Figs. 7b-c and 8d-e), nilas is found within MYI, which is challenging to identify as reported in Dierking (2010). With

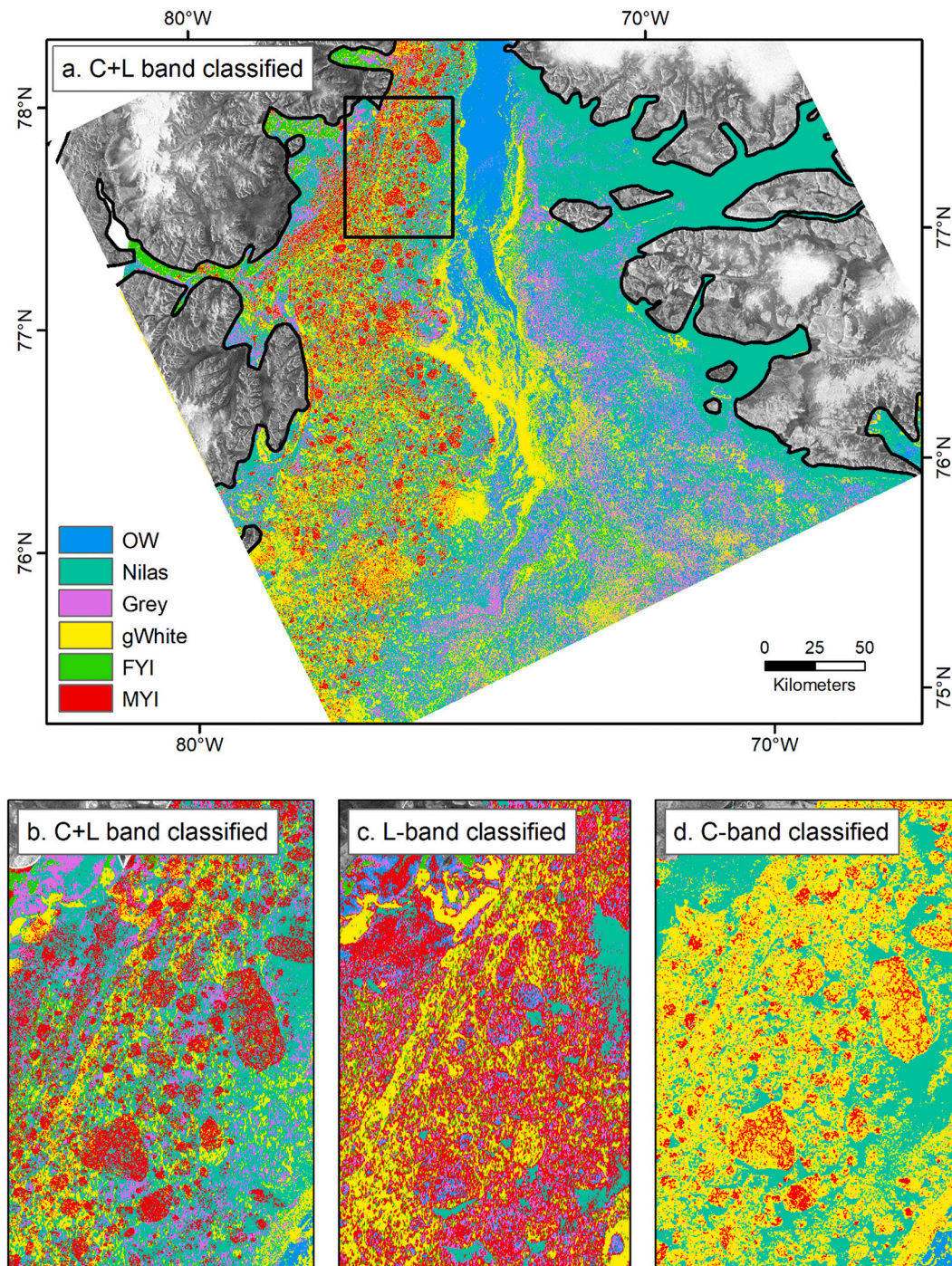


Fig. 10. Classified image from a combination of L- and C-band SAR in NOW. The image extent corresponds to the overlapping areas from C- and L-band imagery. Calibrated L-band SAR scene is shown in the background (a). A comparison of classification performance from C + L, L- and C-band is shown in b-d. Land is outlined in black.

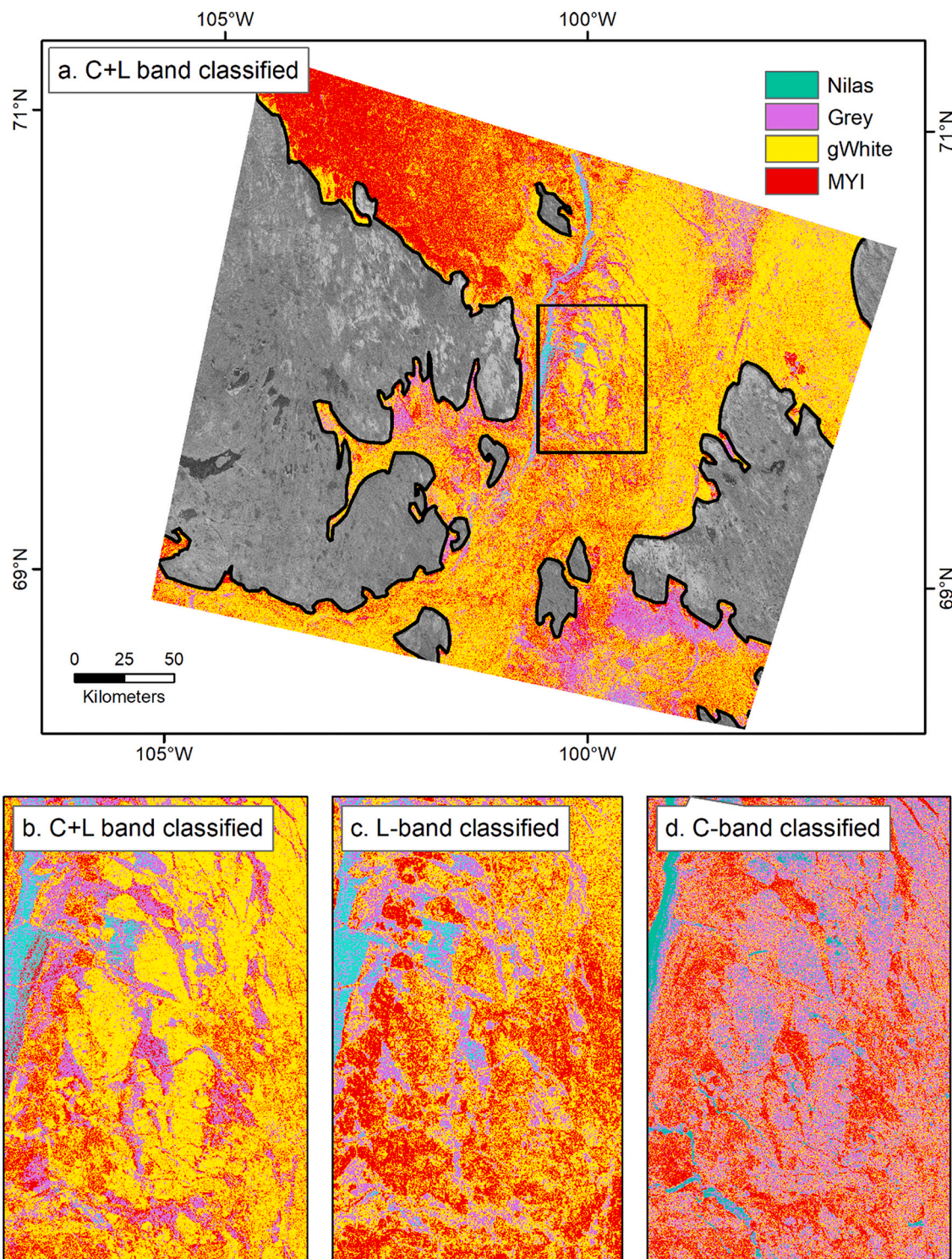


Fig. 11. Same as Fig. 10, but in the Victoria Strait (VS) region.

higher accuracy, the dual-frequency classifier identifies MYI floes within newly formed ice areas (e.g., nilas, grey, gWhite). gWhite and MYI are identified accurately in the dual-frequency classifier, unlike C- or L-band only classifications. For areas with mixed ice classes, a single frequency classification could not identify all classes. Based on our classification results and visual inspection of SAR imagery, we conclude that the dual-frequency classification approach identifies OW and all ice classes more reasonably compared to only C- or L-band outputs.

4.4. Validation and accuracy assessment

We used six transect lines and extracted ice classes for each pixel on transect lines from four classified images and visual inspections to investigate classification performance. The dominant ice classes for different segments on the transect line are shown in Fig. 12.

Transect analysis shows that thinner ice classes (i.e., nilas, grey, gWhite) agree more with visual inspections at L-band than C-band. While L-band captures thinner ice classes in T1e, C-band only identifies

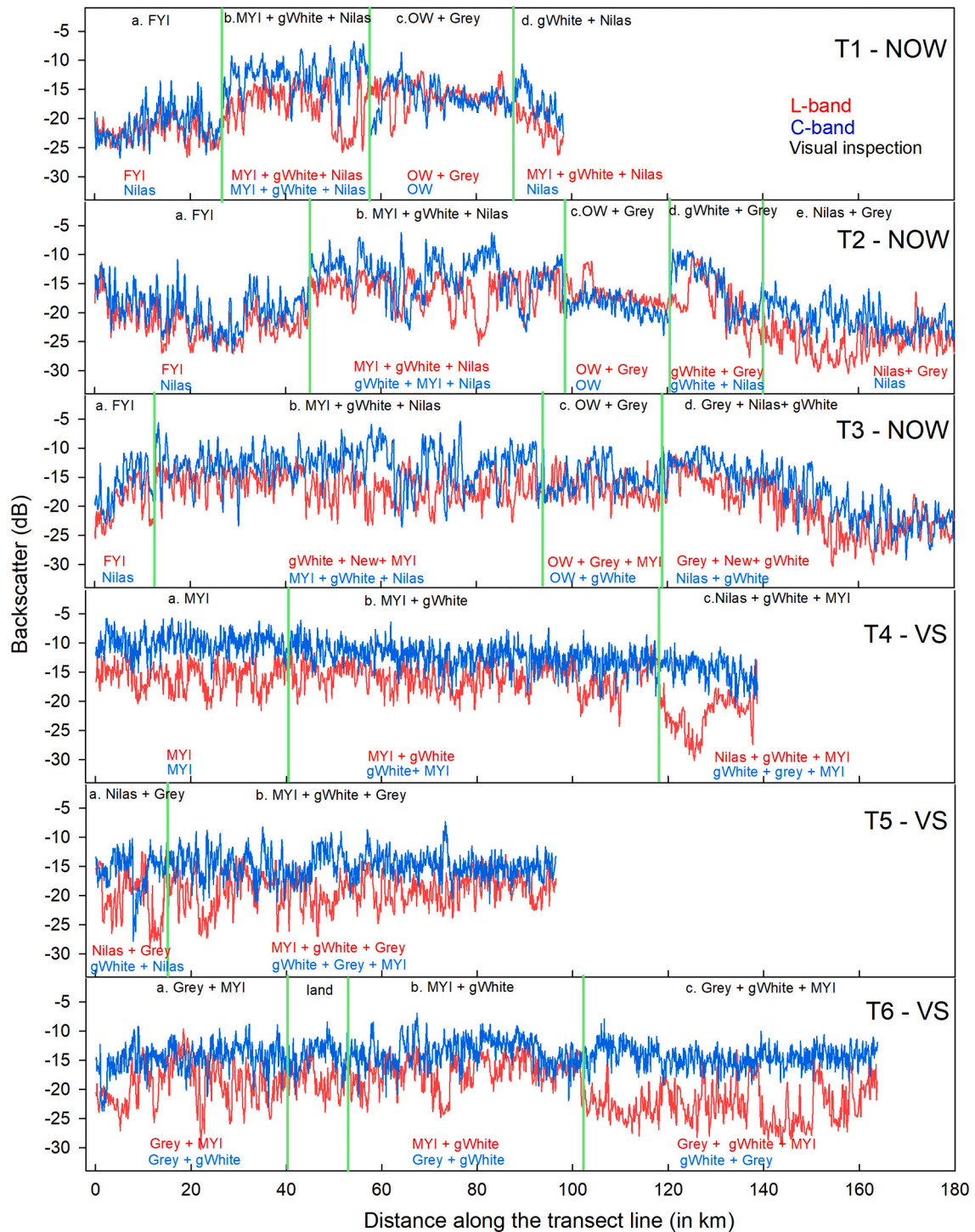


Fig. 12. C- and L-band backscatter coefficient (σ_{HH}^0) are shown on transects lines (e.g., T-1, T-2, ..., T-6) as indicated in Figs. 2 and 3. Transects lines are sub-divided by green lines (e.g., a, b, c etc.) depending on the distribution of major ice classes on the transect lines. According to the dominant ice class, color-coded ice classes are shown for each transect sub-category, followed by second and third dominant ice classes. The ice classes from C- and L-band, shown as blue and red color, are acquired from ice classification outputs as shown in Figs. 6-9, where black color ice classes denote ice-class on transects lines from visual inspections. (For interpretation of the references to color in this figure legend, the reader is referred to the web version of this article.)

nilas. We also find additional MYI identification at L-band at the same segment, which perhaps is misclassified from gWhite. Grey in T1c is reasonably identified at L-band, where grey is misclassified as OW in C-band. In many cases, grey is not identified in C-band (e.g., T1c, T2c, T3c-d, and T5a). L-band identifies the class more reasonably for nilas, where C-band misclassified nilas as grey and gWhite (e.g., T3d, T4c and T5a). We also observed that FYI in T1a is classified as FYI at L-band and nilas

at C-band. Recall tFYI and mFYI are merged as FYI in the classification. Also, we have observed that FYI is misclassified as Nilas at C-band, where L-band identifies FYI in T2a. In T1b, both frequencies perform similarly by identifying MYI, gWhite and nilas, which agree with the visual inspections. However, in T2b, T4b, T5b and T6a-b, MYI is misclassified as gWhite in C-band, where L-band captures the dominant ice class in the segments. MYI dominates T3b via inspection; however, C-

Table 3

Accuracy assessment for image classification from C-band, L-band and both C- and L-band imagery over NOW.

			Classified pixels					
			OW	Nilas	Grey	gWhite	FYI	MYI
			Producer's accuracy (%)					
C-band	Reference pixels (visual inspection)	OW	87	0	8	3	2	0
		Nilas	0	71	4	0	25	0
		Grey	5	12	32	38	13	0
		gWhite	3	2	21	41	6	27
		FYI	3	21	11	9	56	0
		MYI	0	0	13	32	0	55
		User's accuracy (%)	88.8	67	36	33.3	54.9	67.1
		Overall accuracy (%)	57					
		Overall accuracy (%)	57					
L-band	Reference pixels (visual inspection)	OW	81	0	0	3	0	16
		Nilas	0	83	4	13	0	0
		Grey	0	0	85	8	0	7
		gWhite	0	0	17	47	0	36
		FYI	2	5	0	2	91	0
		MYI	0	0	0	9	0	91
		User's accuracy (%)	97.6	94.3	80.2	57.3	100	60.7
		Overall accuracy (%)	79.7					
		Overall accuracy (%)	79.7					
C + L band	Reference pixels (visual inspection)	OW	92	0	0	2	0	6
		Nilas	0	94	2	4	0	0
		Grey	0	0	96	4	0	0
		gWhite	0	1	2	93	0	4
		FYI	0	0	3	1	96	0
		MYI	1	0	0	4	0	95
		User's accuracy (%)	98.9	98.9	93.2	86.1	100	90.5
		Overall accuracy (%)	94.3					
		Overall accuracy (%)	94.3					

band shows gWhite as the dominant ice-class followed by MYI. Perhaps, more MYI is identified as gWhite at C-band since there are similarities in σ_{HH}^0 and GLCM texture parameters among these two classes T3 in Fig. 12 is the most complex area for any classification effort, with a mix of various ice classes in a discrete pattern. At C-band, nilas is confused with FYI (T3a), MYI is confused with gWhite (T3b), grey is confused with gWhite (T3c) and grey ice is not identified (T3d). At L-band, gWhite is mixed with MYI (T3b), OW is identified as MYI (T3c). However, FYI, nilas and grey are reasonably identified at L-band.

Overall, L-band classification accuracy is about 23% higher than C-band. Using 100 from each class, the overall accuracy for C-band classified image is 57% and 56.5% for NOW and VS, respectively (see Tables 3 and 4). OW has the highest accuracy, followed by nilas at C-band. Additionally, grey shows the lowest accuracy (32%) in NOW and gWhite shows the lowest accuracy (27%) in VS. For FYI, the accuracy is 56%. Similar to VS, class-based accuracy for NOW shows that gWhite is underestimated by over 60%, with gWhite misclassified mainly as grey and MYI. At C-band, MYI is classified correctly at 55% and 58% in NOW and VS, respectively, due to misclassification as grey and gWhite. At L-band, the overall accuracy is about 80%. Class-based accuracy shows that MYI is significantly overestimated by 150% in both regions, mainly due to the similar signatures of grey, gWhite and OW. Over two-third of

Table 4

Accuracy assessment for image classification from C-band, L-band and both C- and L-band imagery over VS.

			Classified pixels				
			Nilas	Grey	gWhite	MYI	Producer's accuracy (%)
			Producer's accuracy (%)				
C-band	Reference pixels (visual inspection)	Nilas	85	15	0	0	85
		Grey	0	58	17	21	58
		gWhite	0	53	27	20	27
		MYI	0	14	22	56	56
		User's accuracy (%)	100	41.4	40.9	57.7	
		Overall accuracy (%)	56.5				
		Overall accuracy (%)	56.5				
L-band	Reference pixels (visual inspection)	Nilas	92	7	1	0	92
		Grey	0	79	6	15	79
		gWhite	0	6	63	25	63
		MYI	0	13	7	84	84
		User's accuracy (%)	92	76.1	74.1	76.1	
		Overall accuracy (%)	79.5				
		Overall accuracy (%)	79.5				
C + L band	Reference pixels (visual inspection)	Nilas	98	2	0	0	98
		Grey	0	86	3	11	91
		gWhite	0	4	90	6	93
		MYI	0	7	6	87	87
		User's accuracy (%)	98	86.8	90.9	83.7	
		Overall accuracy (%)	90.3				
		Overall accuracy (%)	90.3				

gWhite areas are classified as grey and MYI. Also, 10–15% of grey are classified as gWhite and MYI. OW, nilas, and FYI class accuracy are over 80%.

When we used both C- and L-band imagery as input to the SVM classifier, the classification accuracy improved substantially. The overall accuracy is 91%. Class-based accuracy shows that gWhite is over-estimated only by about 10%, where grey and MYI contributed 3% and 6%, accordingly. 87% of MYI pixels are accurately classified, with an additional 13% are misclassified from grey, gWhite. Similarly, 8% of OW in NOW region is classified as MYI and gWhite. Higher class accuracy is found for nilas, grey and FYI, where over 90% of reference pixels are accurately classified.

5. Conclusion

We used two coincident pairs of C- and L-band ScanSAR imagery in the North Water (NOW) polynya and Victoria Strait (VS) regions to study new ice types distribution during the freeze-up period. We investigated σ_{HH}^0 and GLCM texture parameters to explore sea ice type separability at C- and L-bands and applied a machine-learning algorithm to perform sea ice type classification.

Results indicated that σ_{HH}^0 for nilas falls very close to the noise floor at both frequencies. As the ice thickens from grey to gWhite ice, C-band σ_{HH}^0 increases but then decreases as the ice thickens to thin and medium FYI. MYI show the highest σ_{HH}^0 at C-band. For L-band, σ_{HH}^0 decreases

from grey ice as sea ice grows into grey-white, thin FYI and medium FYI. MYI shows similar σ_{HH}^0 as grey-white ice. Overall, σ_{HH}^0 at L-band is lower than C-band for all ice types, mainly due to deeper penetration of L-band into ice volume and its lower sensitivity to small-scale surface roughness. Overall, for GLCM texture parameters, C-band shows smaller contrast, larger dissimilarity, higher entropy and less homogeneity than L-band.

We find higher classification accuracy at L-band (about 80%) compared to C-band (about 57%). For the NOW image pair, we find that C-band performed better in identifying OW and MYI, whereas L-band showed improved accuracy in detecting thinner ice classes (e.g., new, grey, gWhite etc.). Signatures of σ_{HH}^0 and GLCM texture parameters for gWhite ice were similar to other ice thinner ice classes at C-band, resulted in lower ice class accuracy. In the case of L-band, MYI showed similarly σ_{HH}^0 and GLCM texture parameters like thinner ice classes; therefore, MYI was over-estimated. Similar results are found from the second image pair acquired over Victoria Strait. For C-band, MYI was under-estimated, grey ice was substantially over-estimated by 42% and gWhite ice was heavily underestimated by 73%. Considering the limitations of C- and L-band only σ_{HH}^0 and GLCM textures, we also used a dual-frequency approach for classification and accuracy improved substantially. The overall accuracy for the dual-frequency approach was substantially higher (e.g., 90.3%) compared to single-frequency approaches. Despite differences in geography, sea ice type distribution, ocean circulation, and atmospheric conditions between NOW and Victoria Strait, the dual-classifier approach produced higher classification accuracy compared to the single-frequency classification. This result highlights the advantages of the dual-frequency classification approach for sea ice monitoring during the freeze-up period.

We recognize that developing a global method of sea ice classification is still a challenge for operational ice monitoring in the Arctic region. In this study we dealt with very different ice conditions for our analysis. For example, MYI in both the regions contained MYI advected from the Arctic Ocean; however, MYI in the NOW was comprised of large floes and had a well-defined boundary edges, whereas MYI in VS contained both MYI that had grown in situ (i.e., FYI that survived the summer melt season and graduated to MYI within the CAA) and MYI that went through several freezes and thaw cycles and was more broken up while moving southward through the CAA.

This contrast in MYI made its identification using only C-band a challenge, and thus, we needed to modify the algorithm to optimize classification performance. To identify the best rule-based classifier, further investigation on backscatter and GLCM parameter variability of ice classes from different Arctic regions using C- and L-band data is required. Despite changing the rule-based decisions in the classifier for VS, it is clear that improved sea ice classification accuracy can be achieved using a dual-frequency approach. However, this also points out that high accuracy sea ice classification still requires some human intervention by adapting ice conditions into the classifier.

This study provides enhanced baseline information on C- and L-band backscatter signatures during Arctic sea ice freeze-up season, which could also help monitor the Antarctic sea ice, where new ice is the dominant ice class. Findings from this study should prove useful forthcoming L-band SAR missions, including NASA-ISRO's NISAR, JAXA's PALSAR-3, ESA's future high-priority ROSE-L and DLR's proposed Tandem-L for cryosphere-climate studies.

Credit author statement

Mallik S. Mahmud: Conceptualization, Methodology, Investigation, Analysis, Visualization, Writing - Original draft preparation, review and editing.

Vishnu Nandan: Analysis, Writing - Review & Editing.

Suman Singha: Methodology.

Stephen E.L. Howell: Methodology, Investigation, Writing - Review & Editing.

Torsten Geldsetzer: Analysis, Writing - Review & Editing.

John Yackel: Supervision, Writing - Review & Editing.

Benoit Montpetit: Analysis, Writing - Review & Editing.

Declaration of Competing Interest

The authors declare that they have no known competing financial interests or personal relationships that could have appeared to influence the work reported in this paper.

Acknowledgement

This work is supported by the NSERC PDF, MEOPAR PDF, Mitacs, Environment and Climate Change Canada contract No. 3000724825 to M. Mahmud. V. Nandan was supported by Julianne Stroeve, the University of Manitoba, in part thanks to funding from the Canada-150 Research Chairs Program in Climate Sea Ice Coupling. J. Yackel is supported by an NSERC Discovery Grant. The authors would like to thank Japan Aerospace Exploration Agency (JAXA), Alaska Satellite Facility and the Canadian Space Agency (CSA) for providing ALOS-2 PALSAR-2, ALOS PALSAR and RADARSAT-2 imagery, respectively. ALOS PALSAR and ALOS-2 PALSAR-2 dataset ©JAXA/METI 2009, 2016, and RADARSAT-2 Data and Products ©MDA Ltd. 2016 – All Rights Reserved. RADARSAT is an official mark of the Canadian Space Agency. The production of the SMOS sea ice thickness data was funded by the ESA project SMOS & CryoSat-2 Sea Ice Data Product Processing and Dissemination Service, and data on December 19, 2016, obtained from <https://www.meereisportal.de> (grant: REKLIM-2013-04).

References

- Aldenhoff, W., Heuzé, C., Eriksson, L.E.B., 2018. Comparison of ice/water classification in Fram Strait from C- and L-band SAR imagery. *Ann. Glaciol.* 59 (76pt2), 112–123. <https://doi.org/10.1017/aog.2018.7>.
- Arkett, M., Flett, D., De Abreu, R., Clemete-Colon, P., Woods, J., Sea, B., 2008. Evaluating Alos-Palsar for Ice Monitoring – what Can L-band do for the North American Ice Service?, 1 Canadian Ice Service – Meteorological Service of Canada - Environment Canada, Ottawa, pp. 188–191. National Ice Centre – Washington, D. C., United States. Analysis.
- Barber, D., Ledrew, E., 1991. Sea ice discrimination using texture statistics- a multivariate approach. *Photogramm. Eng. Remote. Sens.* 57 (4), 385–395.
- Barber, D.G., Nghiem, S.V., 1999. The role of snow on the thermal dependence of microwave backscatter over sea ice. *J. Geophys. Res.* 104 (C11), 25789. <https://doi.org/10.1029/1999JC900181>.
- Barber, D.G., Reddan, S.P., Ledrew, E.F., 1995. Statistical characterization of the geophysical and electrical properties of snow on Landfast first-year sea ice. *J. Geophys. Res.* 100 (C2), 2673. <https://doi.org/10.1029/94JC02200>.
- Barber, D., Marsden, R., Minnett, P., Ingram, G., Fortier, L., 2001. Physical processes within the North Water (NOW) polynya. *Atmosphere-Ocean* 39 (3), 163–166. <https://doi.org/10.1080/07055900.2001.9649673>.
- Barnhart, K.R., Miller, C.R., Overeem, I., Kay, J.E., 2016. Mapping the future expansion of Arctic open water. *Nat. Clim. Chang.* 6 (3), 280–285. <https://doi.org/10.1038/nclimate2848>.
- Cafarella, S.M., Scharien, R., Geldsetzer, T., Howell, S., Haas, C., Segal, R., Nasonova, S., 2019. Estimation of level and deformed first-Year Sea ice surface roughness in the Canadian Arctic archipelago from C- and L-band synthetic aperture radar. *Can. J. Remote. Sens.* <https://doi.org/10.1080/07038992.2019.1647102>.
- Casey, J.A., Howell, S.E.L., Tivy, A., Haas, C., 2016. Separability of sea ice types from wide swath C- and L-band synthetic aperture radar imagery acquired during the melt season. *Remote Sens. Environ.* 174, 314–328. <https://doi.org/10.1016/j.rse.2015.12.021>.
- Cavaliere, D.J., 1994. A microwave technique for mapping thin sea ice. *J. Geophys. Res.* 99 (C6), 12561. <https://doi.org/10.1029/94jc00707>.
- Caves, R., Williams, D., 2015. RADARSAT-2 Applications Technical Note. <https://mdacoorporation.com/docs/default-source/technical-documents/geospatial-services/rn-tn-53-0076-geolocation-tn-1-3.pdf?sfvrsn=4>.
- Clausi, D.A., 2002. An analysis of co-occurrence texture statistics as a function of grey level quantization. *Can. J. Remote. Sens.* 28 (1), 45–62. <https://doi.org/10.5589/m02-004>.
- Comiso, J., 2012. Large decadal decline of the arctic multi-year ice cover. *J. Clim.* 25 (4), 1176–1193. <https://doi.org/10.1175/JCLI-D-11-00113.1>.
- Crawford, A., Stroeve, J., Smith, A., Jahn, A., 2021. Arctic open-water periods are projected to lengthen dramatically by 2100. *Commun. Earth Environ.* 2 (1), 109. <https://doi.org/10.1038/s43247-021-00183-x>.
- Dabboor, M., Montpetit, B., Howell, S.E.L., Haas, C., Dabboor, M., Montpetit, B., Howell, S.E.L., Haas, C., 2017. Improving Sea ice characterization in dry ice winter

- conditions using polarimetric parameters from C- and L-band SAR data. *Remote Sens.* 9 (12), 1270. <https://doi.org/10.3390/rs9121270>.
- Dierking, W., 2010. Mapping of different sea ice regimes using images from Sentinel-1 and ALOS synthetic aperture radar. *IEEE Trans. Geosci. Remote Sens.* 48 (3), 1045–1058.
- Dierking, Wolfgang, Busche, T., 2006. Sea ice monitoring by L-band SAR: an assessment based on literature and comparisons of JERS-1 and ERS-1 imagery. *IEEE Trans. Geosci. Remote Sens.* 44 (4), 957–970. <https://doi.org/10.1109/TGRS.2005.861745>.
- Dierking, Wolfgang, Dall, J., 2007. Sea-ice deformation state from synthetic aperture radar imagery—part I: comparison of C- and L-band and different polarization. *IEEE Trans. Geosci. Remote Sens.* 45 (11), 3610–3622. <https://doi.org/10.1109/TGRS.2007.903711>.
- Dierking, Wolfgang, Dall, J., 2008. Sea ice deformation state from synthetic aperture radar imagery - Part II: effects of spatial resolution and noise level. *IEEE Trans. Geosci. Remote Sens.* <https://doi.org/10.1109/TGRS.2008.917267>.
- Dierking, W., Pettersson, M.I., Askne, J., 1999. Multifrequency scatterometer measurements of Baltic Sea ice during EMAC-95. *Int. J. Remote Sens.* 20 (2), 349–372. <https://doi.org/10.1080/014316999213488>.
- Else, B.G.T., Papakyriakou, T.N., Galley, R.J., Drennan, W.M., Miller, L.A., Thomas, H., 2007. Wintertime CO₂ fluxes in an Arctic polynya using eddy covariance: evidence for enhanced air-sea gas transfer during ice formation. *J. Geophys. Res.* 116 <https://doi.org/10.1029/2010JC006760>, 0–03.
- Geldsetzer, T., Yackel, J., 2009. Sea ice type and open water discrimination using dual co-polarized C-band SAR. *Can. J. Remote. Sens.* 35 (1), 73–84. <https://doi.org/10.5589/m08-075>.
- Grosfeld, K., Treffeisen, R., Asseng, J., Bartsch, A., Bräuer, B., Fritsch, B., Gerdes, R., Hendricks, S., Hiller, W., Heygster, G., Krumpen, T., Lemke, P., Melheimer, C., Nicolaus, M., Ricker, R., Weigelt, M., 2016. Online sea-ice knowledge and data platform <www.meereisportal.de>. *Polarforschung, Bremerhaven, Alfred Wegener Institute for Polar and Marine Research & German Society of Polar Research* 85 (2), 143–155.
- Haralick, R.M., Shanmugam, K., Dinstein, L.H., 1973. Textural features for image classification. *IEEE Trans. Syst. Man Cybernet.* 6, 610–621.
- Howell, S.E., Tivy, A., Yackel, J.J., Else, B.G., Duguay, C.R., 2008. Changing sea ice melt parameters in the Canadian Arctic Archipelago: implications for the future presence of multi-year ice. *J. Geophys. Res. Ocean* 113 (C9).
- Howell, S.E.L., Komarov, A.S., Dabboor, M., Montpetit, B., Brady, M., Scharien, R.K., Mahmud, M.S., Nandan, V., Geldsetzer, T., Yackel, J.J., 2018. Comparing L- and C-band synthetic aperture radar estimates of sea ice motion over different ice regimes. *Remote Sens. Environ.* 204, 380–391. <https://doi.org/10.1016/j.rse.2017.10.017>.
- Howell, S.E.L., Small, D., Rohner, C., Mahmud, M.S., Yackel, J.J., Brady, M., 2019. Estimating melt onset over Arctic Sea ice from time series multi-sensor Sentinel-1 and RADARSAT-2 backscatter. *Remote Sens. Environ.* <https://doi.org/10.1016/j.rse.2019.04.031>.
- Inman, H.F., Bradley Jr., E.L., 1989. The overlapping coefficient as a measure of agreement between probability distributions and point estimation of the overlap of two normal densities. *Commun. Stat. Theor. Methods* 18 (10), 3851–3874.
- Isleifson, D., Hwang, B., Barber, D.G., Scharien, R.K., Shafai, L., 2010. C-band polarimetric backscattering signatures of newly formed sea ice during fall freeze-up. *IEEE Trans. Geosci. Remote Sens.* 48 (8), 3256–3267. <https://doi.org/10.1109/TGRS.2010.2043954>.
- Isleifson, D., Galley, R.J., Barber, D.G., Landy, J.C., Komarov, A.S., Shafai, L., 2014. A study on the c-band polarimetric scattering and physical characteristics of frost flowers on experimental sea ice. *IEEE Trans. Geosci. Remote Sens.* 52 (3), 1787–1798. <https://doi.org/10.1109/TGRS.2013.2255060>.
- Jansen, E., Christensen, J.H., Dokken, T., Nisanoglu, K.H., Vinther, B.M., Capron, E., Guo, C., Jensen, M.F., Langen, P.L., Pedersen, R.A., Yang, S., Bentsen, M., Kjær, H.A., Sadatzki, H., Sessford, E., Stendel, M., 2020. Past perspectives on the present era of abrupt Arctic climate change. *Nat. Clim. Chang.* 10 (8), 714–721. <https://doi.org/10.1038/s41558-020-0860-7>.
- Johansson, A.M., King, J.A., Douglis, A.P., Gerland, S., Spreen, G., Busche, T., 2017. Combined observations of Arctic sea ice with near-coincident colocated X-band, C-band, and L-band SAR satellite remote sensing and helicopter-borne measurements. *J. Geophys. Res. Oceans* 122 (1), 669–691. <https://doi.org/10.1002/2016JC012273>.
- Johansson, A., Malin, Brekke, C., Spreen, G., King, J.A., 2018. X-, C-, and L-band SAR signatures of newly formed sea ice in Arctic leads during winter and spring. *Remote Sens. Environ.* 204, 162–180. <https://doi.org/10.1016/j.rse.2017.10.032>.
- Kaleschke, L., Tian-Kunze, X., Maaß, N., Mäkynen, M., Drusch, M., 2012. Sea ice thickness retrieval from SMOS brightness temperatures during the Arctic freeze-up period. *Geophys. Res. Lett.* 39 (5) <https://doi.org/10.1029/2012GL050916>.
- Kankaku, Y., Osawa, Y., Suzuki, S., Watanabe, T., 2009. The overview of the L-band SAR onboard ALOS-2. In: *Proceedings of Progress in Electromagnetics Research Symposium*, 2, pp. 735–738. In: <https://piers.org/papers/proceedings/download.php?file=GllcnMyMDA5TW9yZy293fDNQMv8wNzM1LnBkZnwwOTAYMTgYMTAzMtU>.
- Keller, M.R., Gifford, C.M., Winstead, N.S., Walton, W.C., Dietz, J.E., 2020. Active/passive multiple polarization sea ice detection during initial freeze-up. *IEEE Trans. Geosci. Remote Sens.* 59 (7), 5434–5448. <https://doi.org/10.1109/tgrs.2020.3013512>.
- Kim, Y.S., Moore, R.K., Onstott, R.G., 1984. *Theoretical and Experimental Study of Radar Backscatter from Sea Ice*. Remote Sensing Laboratory Center for Research, University of Kansas. RSL Technical Report RSL TR 331-37.
- Kwok, R., 2018. Arctic sea ice thickness, volume, and multi-year ice coverage: losses and coupled variability (1958–2018). *Environ. Res. Lett.* 13 (10), 105005. <https://doi.org/10.1088/1748-9326/aae3ec>.
- Kwok, R., Nghiem, S.V., Martin, S., Winebrenner, D.P., Gow, A.J., Perovich, D.K., Swift, C.T., Barber, D.G., Golden, K.M., Knapp, E.J., 1998. Laboratory measurements of sea ice: connections to microwave remote sensing. *IEEE Trans. Geosci. Remote Sens.* 36 (5), 1716–1730. <https://doi.org/10.1109/36.718640>.
- Liu, H., Guo, H., Zhang, L., 2015. SVM-based sea ice classification using textural features and concentration from RADARSAT-2 dual-pol ScanSAR data. *IEEE J. Sel. Top. Appl. Earth Obs. Remote Sens.* 8 (4), 1601–1613. <https://doi.org/10.1109/JSTARS.2014.2365215>.
- Mahmud, Mallik Sezan, Howell, S.E.L., Geldsetzer, T., Yackel, J., 2016. Detection of melt onset over the northern Canadian Arctic Archipelago sea ice from RADARSAT, 1997–2014. *Remote Sens. Environ.* 178, 59–69. <https://doi.org/10.1016/j.rse.2016.03.003>.
- Mahmud, Mallik S., Geldsetzer, T., Howell, S.E.L., Yackel, J.J., Nandan, V., Scharien, R. K., 2018. Incidence angle dependence of HH-polarized C- and L-band wintertime backscatter over arctic sea ice. *IEEE Trans. Geosci. Remote Sens.* 1–13. <https://doi.org/10.1109/TGRS.2018.2841343>.
- Mahmud, Mallik S., Nandan, V., Howell, S.E.L., Geldsetzer, T., Yackel, J., 2020. Seasonal evolution of L-band SAR backscatter over landfast Arctic sea ice. *Remote Sens. Environ.* 251, 112049. <https://doi.org/10.1016/j.rse.2020.112049>.
- Maykut, G.A., 1982. Large-scale heat exchange and ice production in the Central Arctic. *J. Geophys. Res.* 87 (C10), 7971. <https://doi.org/10.1029/JC087iC10p07971>.
- Melling, H., 2002. Sea ice of the northern Canadian Arctic Archipelago. *J. Geophys. Res. Oceans* 107 (C11), 2–1.
- Melling, H., Gratton, Y., Ingram, G., 2001. Ocean circulation within the North Water polynya of Baffin Bay. *Atmosphere-Ocean* 39 (3), 301–325. <https://doi.org/10.1080/07055900.2001.9649683>.
- Moore, G.W.K., Howell, S.E.L., Brady, M., Xu, X., McNeil, K., 2021. Anomalous collapses of Nares Strait ice arches leads to enhanced export of Arctic sea ice. *Nat. Commun.* 12 (1), 1–8. <https://doi.org/10.1038/s41467-020-20314-w>.
- Mundy, C.J., Barber, D.G., 2001. On the relationship between spatial patterns of sea-ice type and the mechanisms which create and maintain the North Water (NOW) polynya. *Atmosphere-Ocean* 39 (3), 327–341. <https://doi.org/10.1080/07055900.2001.9649684>.
- Murashkin, D., Spreen, G., Huntemann, M., Dierking, W., 2018. Method for detection of leads from Sentinel-1 SAR images. *Ann. Glaciol.* 59 (76pt2), 124–136.
- Nghiem, S.V., Martin, S., Perovich, D.K., Kwok, R., Drucker, R., Gow, A.J., 1997. A laboratory study of the effect of frost flowers on C band radar backscatter from sea ice. *J. Geophys. Res. C: Ocean* 102 (C2), 3357–3370. <https://doi.org/10.1029/96JC03208>.
- Ochilov, S., Clausi, D.A., 2012. Operational SAR sea-ice image classification. *IEEE Trans. Geosci. Remote Sens.* 50 (11 PART1), 4397–4408. <https://doi.org/10.1109/TGRS.2012.2192278>.
- Onstott, R.G., 1992. SAR and scatterometer signatures of sea ice. In: Carsey, F. (Ed.), *Microwave Remote Sensing of Sea Ice*. American Geophysical Union, pp. 73–104. *Geophysics*.
- Ressel, R., Frost, A., Lehner, S., 2015. A neural network-based classification for sea ice types on X-band SAR images. *IEEE J. Sel. Top. Appl. Earth Obs. Remote Sens.* 8 (7), 3672–3680. <https://doi.org/10.1109/JSTARS.2015.2436993>.
- Ressel, R., Singha, S., Lehner, S., Rosel, A., Spreen, G., 2016. Investigation into different polarimetric features for sea ice classification using X-band synthetic aperture radar. *IEEE J. Sel. Top. Appl. Earth Obs. Remote Sens.* 9 (7), 3131–3143. <https://doi.org/10.1109/JSTARS.2016.2539501>.
- Scharien, R.K., Nasonova, S., 2020. Incidence angle dependence of texture statistics from Sentinel-1 HH-polarization images of winter Arctic sea ice. *IEEE Geosci. Remote Sens. Lett.* <https://doi.org/10.1109/LGRS.2020.3039739>.
- Scharien, Randall K., Geldsetzer, T., Barber, D.G., Yackel, J., Langlois, A., 2010. Physical, dielectric, and C band microwave scattering properties of first-year sea ice during advanced melt. *J. Geophys. Res. Oceans* 115 (12), 1–16. <https://doi.org/10.1029/2010JC006257>.
- Scharien, Randall K., Segal, R., Nasonova, S., Nandan, V., Howell, S.E.L., Haas, C., 2017. Winter Sentinel-1 backscatter as a predictor of spring Arctic sea ice melt pond fraction. *Geophys. Res. Lett.* <https://doi.org/10.1002/2017GL075547>.
- Shokr, M.E., 1991. Evaluation of second-order texture parameters for sea ice classification from radar images. *J. Geophys. Res.* 96 (C6), 10625. <https://doi.org/10.1029/91JC00693>.
- Singha, S., Johansson, M., Hughes, N., Hvidegaard, S.M., Skourup, H., 2018. Arctic sea ice characterization using spaceborne fully polarimetric L-, C-, and X-band SAR with validation by airborne measurements. *IEEE Trans. Geosci. Remote Sens.* 56 (7), 3715–3734. <https://doi.org/10.1109/TGRS.2018.2809504>.
- Soh, L.K., Tsatsoulis, C., 1999. Texture analysis of SAR sea ice imagery using gray level co-occurrence matrices. *IEEE Trans. Geosci. Remote Sens.* 37 (2), 780–795.
- Stroeve, J., Notz, D., 2018. Changing state of Arctic sea ice across all seasons. *Environ. Res. Lett.* 13 (10), 103001. <https://doi.org/10.1088/1748-9326/AADE56>.
- Tian-Kunze, X., Kaleschke, L., Maaß, N., Mäkynen, M., Serra, N., Drusch, M., Krumpen, T., 2014. SMOS-derived thin sea ice thickness: algorithm baseline, product specifications and initial verification. *Cryosphere* 8, 997–1018.
- Tivy, A., Howell, S.E.L., Alt, B., McCourt, S., Chagnon, R., Crocker, G., Carrieres, T., Yackel, J., 2011. Trends and variability in summer sea ice cover in the Canadian Arctic based on the Canadian Ice Service Digital Archive, 1960–2008 and 1968–2008. *J. Geophys. Res. Oceans* 116 (3). <https://doi.org/10.1029/2009JC005855>.
- Toyota, T., Ishiyama, J., Kimura, N., 2020. Measuring deformed sea ice in seasonal ice zones using L-band SAR images. *IEEE Trans. Geosci. Remote Sens.* 59 (11), 9361–9381. <https://doi.org/10.1109/TGRS.2020.3043335>.
- Tucker, W.B., Perovich, D.K., Gow, A.J., Weeks, W.F., Drinkwater, M.R., 1992. Physical properties of sea ice relevant to remote sensing. In: *Microwave Remote Sensing of Sea Ice*, pp. 9–28. <https://doi.org/10.1029/GM068p0009>.

- Ulaby, F.T., Moore, R.K., Fung, A.K., 1981. Microwave Remote Sensing: Active and Passive. Volume 1 - Microwave Remote Sensing Fundamentals and Radiometry. United States. <https://ntrs.nasa.gov/search.jsp?R=19820039342>.
- Vapnik, V., Levin, E., Cun, Y.Le., 1994. Measuring the VC-dimension of a learning machine. Neural Comput. 6 (5), 851–876. <https://doi.org/10.1162/neco.1994.6.5.851>.
- Winebrenner, D.P., Nelson, E.D., Colony, R., West, R.D., 1994. Observation of melt onset on multi-year Arctic sea ice using the ERS 1 synthetic aperture radar. J. Geophys. Res. 99 (C11), 22425. <https://doi.org/10.1029/94JC01268>.
- Yackel, J., Barber, D.G., 2000. Melt ponds on sea ice in the Canadian Archipelago: 2. On the use of RADARSAT-1 synthetic aperture radar for geophysical inversion. J. Geophys. Res. Oceans 105 (C9), 22061–22070. <https://doi.org/10.1029/2000JC900076>.
- Zakhvatkina, N., Smirnov, V., Bychkova, I., 2019. Satellite SAR data-based sea ice classification: an overview. Geosciences 9 (4), 152. <https://doi.org/10.3390/geosciences9040152>.